

Fakultät für Physik und Astronomie
Ruprecht-Karls-Universität Heidelberg

Diplomarbeit
im Studiengang Physik

vorgelegt von
Felix Frank

aus Lahr

2007

Comparison of Two Femtosecond Laser Systems For Two-Photon Imaging of RPE Cells

Die Diplomarbeit wurde von Felix Frank ausgeführt am
Kirchhoff Institut für Physik
unter der Betreuung von
Herrn Prof. Dr. J. Bille

Abstract

Age-related macular degeneration (AMD) is a retinal disease that affects the retinal pigment epithelium (RPE) cells in the macular region. It is the leading cause for blindness in the Western world. In the RPE, enlarged lipofuscin granules show autofluorescence that is monitored through confocal scanning laser ophthalmoscope (cSLO) in clinical practice today.

This work focuses on a new approach. The lipofuscin is imaged by means of a two-photon excited fluorescence (TPEF) ophthalmoscope. This offers intrinsic three dimensional resolution and a larger sensing depth. A conventional cSLO (HRT, Heidelberg Engineering, Germany) has been modified for TPEF imaging at video rate speed (20 Hz).

Two different femtosecond (fs) lasers have been used for the setup. A mode-locked Ti:Sa laser (Mira 900, Coherent, USA) and a compact, all diode-pumped, solid-state Nd:glass fsd oscillator (*femto*TRAINTM Nd-Glas V1.0, High Q Laser, Austria).

The first images of the high-speed TPEF ophthalmoscope on retinas from donor eyes are presented. The results show the potential for *in vivo* TPEF imaging of the human eye in everyday clinical use.

Zusammenfassung

Altersbedingte makuläre Degeneration (AMD) ist eine Netzhauterkrankung, welche die Pigmentepithelzellen (RPE) in der Makula beeinträchtigt. In den RPE Zellen zeigen vergrößerte Lipofuscin Körnchen Autofluoreszenz, die heutzutage in den Kliniken mit einem konfokalen Scanning Laser Ophthalmoskop (cSLO) kontrolliert wird.

In dieser Arbeit wird ein neuer Ansatz verfolgt. Das Lipofuscin wird durch ein Zwei-Photonen Fluoreszenz (TPEF) Ophthalmoskop beobachtet. Das erlaubt intrinsische dreidimensionale Auflösung und eine größere Ablesetiefe. Ein konventionelles cSLO (HRT, Heidelberg Engineering, Germany) wurde umgebaut um TPEF Bildgebung in Videogeschwindigkeit (20 Hz) darzustellen. Zwei unterschiedliche Femtosekunden (fs) Laser wurden für den Aufbau verwendet. Ein modengekoppelter Ti:Sa Laser (Mira900, Coherent, USA) und ein kompakter, diodengepumpter Nd:glas fs-Oszillator (*femto*TRAINTM Nd-Glas V1.0, High Q Laser, Austria).

Es werden die ersten Bilder des Video TPEF Ophthalmoskop von Spender-Netzhäuten gezeigt. Die Ergebnisse zeigen Potential für *in vivo* TPEF Bildgebung am menschlichen Auge im Klinikalltag.

Contents

1	Introduction	1
2	Ultrafast Lasers	3
2.1	Q Switching	3
2.2	Mode-Locking	4
2.3	Saturable Absorbers	8
2.3.1	SESAM	9
2.3.2	KLM	10
2.4	Propagation of Ultrashort Pulses	12
2.5	GVD Compensation	15
2.5.1	Prism Pairs	15
2.5.2	Dispersive Mirrors	16
2.6	Self Phase Modulation	16
3	Fundus Microscopy	19
3.1	The cSLO	19
3.2	Non Linear Microscopy	22
3.2.1	Two Photon Excited Microscopy	23
3.2.2	SHG Microscopy	25
4	The Eye	27
4.1	Anatomy	27
4.2	Properties of the Retina	28
4.3	The Optics of the Eye	30
4.3.1	The Reduced Eye	31
4.3.2	The Gullstrand-Le Grand Eye	31
4.4	Ametropia	33
4.4.1	Hyperopia	33
4.4.2	Myopia	33
4.5	Fundus Reflectance	34
4.5.1	Reflectors of the Fundus	34

4.5.2	Absorbers of the Fundus	35
4.6	Cataract	36
4.7	AMD	37
4.8	Lipofuscin	38
5	Results	41
5.1	Materials and Methods	41
5.1.1	Optical Setup	41
5.1.2	Sample Preparation	43
5.2	Image Comparison	43
5.2.1	Images from the TP Ophthalmoscope	43
5.2.2	Comparing Fluorescence Efficiency	45
5.2.3	Comparison With a Slow-scanning Microscope	47
5.2.4	Laser Safety	49
6	Summary and Discussion	51
A	Resonator Stability	55
A.1	Ray Matrix	55
A.2	Paraxial Wave Equation	55
A.3	Gaussian Beams	57
A.4	Stable Resonators	59
A.5	Resonator Stability	60
B	Nonlinear Effects	61
B.1	Frequency Doubling	61
B.2	Polarization and Susceptibility	61
B.3	Wave Equation	62
B.4	Frequency Doubling	62
	Bibliography	64
	List of Figures	74

Chapter 1

Introduction

Age-related macular degeneration (AMD) is a retinal disease that affects the retinal pigment epithelium (RPE) cells in the macular region and leads to a degeneracy in the function of photoreceptors. It is the leading cause for blindness in the Western world. Much effort is therefore put into the understanding of this disease. The development of novel in vivo diagnostic tools is important to understand the disease on a subcellular level.

The RPE cells are located between the neurosensory part of the retina and Bruch's membrane. They play a key role in the metabolism of the retina. These cells account for many special needs and are considered as nurse cells of the retina. RPE cells remove toxic molecules and free radicals, they transport nutrients to the neurosensory part and protect the fragile photoreceptors from highly energetic low-wavelength light. They also take part in the biosynthesis of A2E and are thereby closely related to the formation and accumulation of lipofuscin in the free cytoplasmic space of the RPE cells. The amount and spatial distribution of the autofluorescent lipofuscin is closely related to AMD gives an insight to the pathogenesis of retinal diseases [1–5]. Today, fundus autofluorescence (FAF) is imaged with modified fundus cameras or confocal scanning laser ophthalmoscopes [6–9]. The lipofuscin granules can be excited with blue light. The amount and also the change over time of the fluorescence gives an indication how AMD progresses [10].

In this thesis a noninvasive method for retina imaging is described. By means of a two-photon excited fluorescence (TPEF) ophthalmoscope the RPE cells are imaged. The basic principle behind this approach is the use of two photons interacting with a fluorophore, producing an excitation equivalent to the absorption of a single photon possessing twice the energy. Since the first realization of a TPEF microscope by Denk *et al.* this method has become more and more important in the biological science [11]. It has many advantages over single-photon microscopy. For one, the use of near infrared

light (NIR) is less harmful to cells than UV light that would have to be used in single-photon excitation. UV light is more energetic and can kill cells by damaging their DNA. NIR light is also more suitable to image thicker samples due to less scattering and the lack of endogenous absorbers in this spectral range [12–14]. Another advantage is the intrinsic three-dimensional resolution that results from the quadratic dependence on the intensity of the illumination light. This allows for optical sectioning of the quite thick retina. In addition it also reduces photobleaching to the focal plane instead of the whole illumination cone like in conventional single-photon imaging.

This thesis focuses on the development and characterization of a high-speed laser-scanning ophthalmoscope (20 frames per second). Fast resonant scanning systems are needed for *in vivo* diagnostic methods to minimize the influence of eye movements on the image quality. Besides reducing artifacts from eye-movements, fast scanning can also contribute to a fluorescence signal increase by relaxation of molecular dark states in between two absorption events. This was introduced by Borlinghaus and Donnert *et al.* and has yet to be discussed in laser scanning ophthalmoscopes [15, 16].

Chapter 2

Ultrafast Lasers

Ultrafast lasers have dramatically changed over the last decade. They used to be complicated systems that were operated in specialized laboratories, but are now available as ‘turn-key’ products with compact designs. Diode pumped lasers, new lasing materials and fast saturable absorbers, based on the Kerr effect¹ or on semiconductor devices, have boosted their performance and reliability. There are now many ultrafast lasers sources for many different applications available. Laser pulse generation started as early as 1966, only six years after the first demonstration of a laser. De Maria *et al.* produced the first pulses using a passively modelocked Nd:glass laser, generating picosecond pulses [17]. Figure 2.1 shows the evolution of ultrafast lasers ever since. In the early times usually dye lasers were used to achieve ultrashort pulses. With the discovery of the broad gain width medium Ti:Sapphire [18] and its inherent saturable absorber (KLM), a new era started.

2.1 Q Switching

Q switching is a way of obtaining short laser pulses. The name comes from the quality factor Q used for laser resonators. A high-Q cavity has low losses and vice versa [21]. The generation of pulses is introduced by keeping the losses of the resonator high for a time. This results in a highly populated upper state of the laser medium, limited by spontaneous emission. Then the losses are reduced to allow lasing, thus Q-switching. Consequently the intensity in the resonator increases very fast, leading to a large stimulated emission. An intense pulse is being formed, as short as 10^{-9} s. Figure 2.2 illustrates this process. There are many methods introducing those artificial intra-cavity losses. The most common ones are saturable absorbers (*passive*)

¹usually referred to as Kerr Lens Modelocking (KLM)

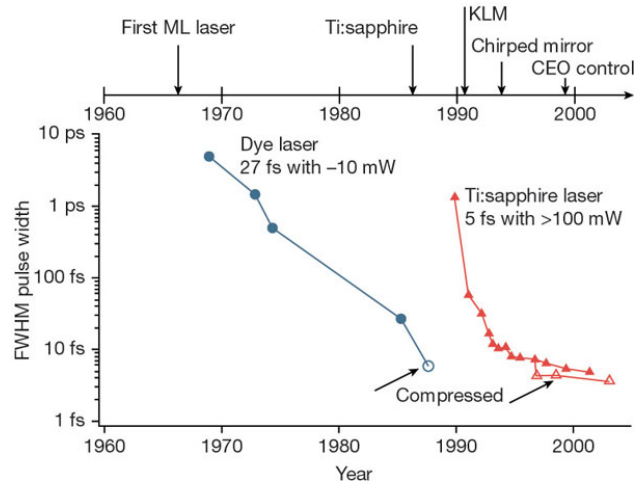


Figure 2.1: Improvements in ultrashort pulse generation. Until the late 1980's dye lasers were used, reaching pulse lengths as short as 27 fs (even 6 fs with external pulse compression). The discovery of Ti:Sapphire as a laser medium gave new alternatives to reach even smaller pulse width in the sub-two cycle regime [19]. Filled symbols indicate results directly achieved from a laser and open symbols are achieved with additional external compression [20]

and electro-optical (*active*) switches. With this method, the *ultrafast* regime is not yet reached. Different things have to be taken into account to reach the femtosecond limit. But before getting to shorter pulses I will now describe how a pulse is formed in the resonator.

2.2 Mode-Locking

Ultrashort pulses are generated by mode-locked lasers. A short pulse is formed by constructive interference when many longitudinal modes are held in phase in a laser resonator. All of the longitudinal modes satisfy the standing wave condition $n\lambda = 2L$, where n is a positive integer and L the length of the cavity. The frequency separation is determined by adding half a wavelength ($n \rightarrow n + 1$) and is given by:

$$\Delta\nu = \frac{c}{2L} \quad (2.1)$$

Just like the transverse modes, the amplification of longitudinal modes leads to statistical fluctuations of the intensity. If now the phase of each mode is locked together, $\Phi_{m+1} - \Phi_m = \alpha$, pulses are generated as a superposition of

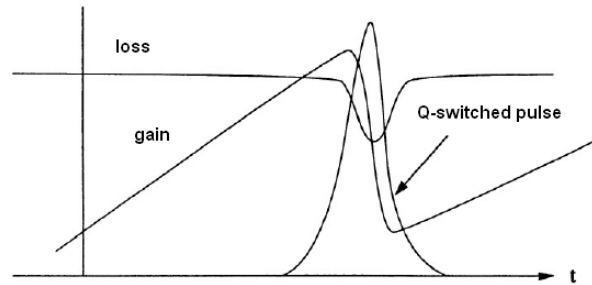


Figure 2.2: Q-switching: The loss is controlled to prevent lasing, until the gain is saturated. Notice how the gain rapidly decreases, as soon as the lasers starts. It doesn't rise until the pump mechanism is larger than the depletion.

each mode. For $\alpha = 0$ and $2N + 1$ modes, the superposition of them can be written as:

$$\vec{E}(t) = \sum_{m=-N}^N \vec{E}_0 e^{2\pi i(\nu_0 + m\Delta\nu)t} \quad (2.2)$$

where ν_0 is the middle frequency. The intensity, i.e. the square of the absolute value of Equation 2.2, can then be written asⁱⁱ [21, 22]:

$$I(t) \propto \left(\frac{\sin[(2N+1)(\pi \Delta\nu t)]}{\sin(\pi \Delta\nu t)} \right)^2 \quad (2.3)$$

In Figure 2.3 the intensity for seven locked modes is shown. At $t = 0$ and $t = T = \frac{2L}{c}$ the superposition of those modes lead to a maximum. There are $n-2$ side-maxima between the main maxima. They travel with light velocity, thus only one pulse is traveling in the cavity. The maxima get sharper if more modes are involved and can be estimated as $\tau_N = \frac{T}{N}$, as is demonstrated in Figure 2.3. The total number of modes that are supported by any laser medium is determined by the gain linewidth $\Delta\nu_g$ and the frequency separation $c/2L$. Assuming sufficiently strong pumping the total number of longitudinal modes is given by $\# \text{ modes} = \frac{\Delta\nu_g}{c/2L}$ and thus the shortest pulse duration one can expect is:

$$\tau_{min} \approx \frac{1}{\Delta\nu_g} \quad (2.4)$$

From this equation you can see the need for broadband laser materials in

ⁱⁱusing the identity: $\sum_{n=-(N-1)/2}^{(N-1)/2} e^{iny} = \frac{\sin(Ny/2)}{\sin(y/2)}$

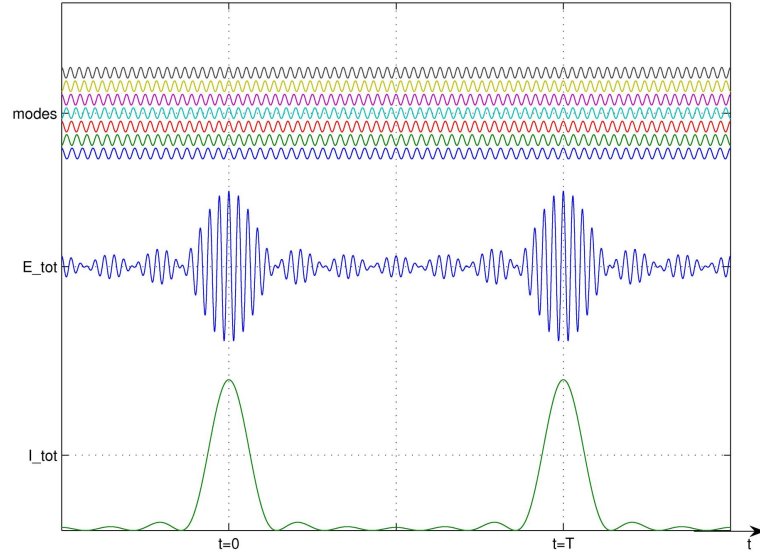


Figure 2.3: The locking of 7 modes. You can see the superposition of the electric field and the resulting intensity.

order to generate a small pulse. One can calculate the temporal profile of a fully modelocked pulse by using the Fourier transform of the spectrum. The exact correlation between the pulsewidth and the width of the spectrum depends on the form of the pulse. For a Gaussian pulse, the calculations are straight forward.

Assume an intensity distribution with a FWHM of τ , then $I(t) = I_0 \exp\left[-4 \ln 2 \left(\frac{t}{\tau}\right)^2\right]$ and by Fourier transformation, one gets the spectrum:

$$\begin{aligned}
 \tilde{I}(\nu) &= \mathcal{F}[I(t)] = \int I(t) e^{-2\pi i \nu t} dt \\
 &= \int \exp\left[-4 \ln 2 \frac{t^2}{\tau^2} - 2\pi i \nu t\right] dt \\
 &= \exp\left[\frac{-\beta^2}{\alpha^2}\right] \int e^{-x^2} dx = \sqrt{\pi} \exp\left[\frac{-\beta^2}{\alpha^2}\right] \\
 \tilde{I}(\nu) &= \sqrt{\pi} \exp\left[\frac{-4\pi^2 \nu^2 \tau^2}{4 \ln 2}\right]
 \end{aligned}$$

where $\alpha^2 = \frac{2 \ln 2}{\tau^2}$, $\beta = \frac{\pi \nu}{\alpha}$ and $x = \alpha t + i \frac{\beta}{\alpha}$ to get the standard Gaußintegral. The FWHM of $\tilde{I}(\nu)$ can easily be determined to be $\Delta \nu \cdot \tau = \frac{2 \ln 2}{\pi} \approx 0.441$

The constant obtained in the calculations above is different for every pulse shape. A secans hyperbolicus shape is of special interest here, as it approximates a fs-pulse quite well. The same calculations as above lead to a slightly

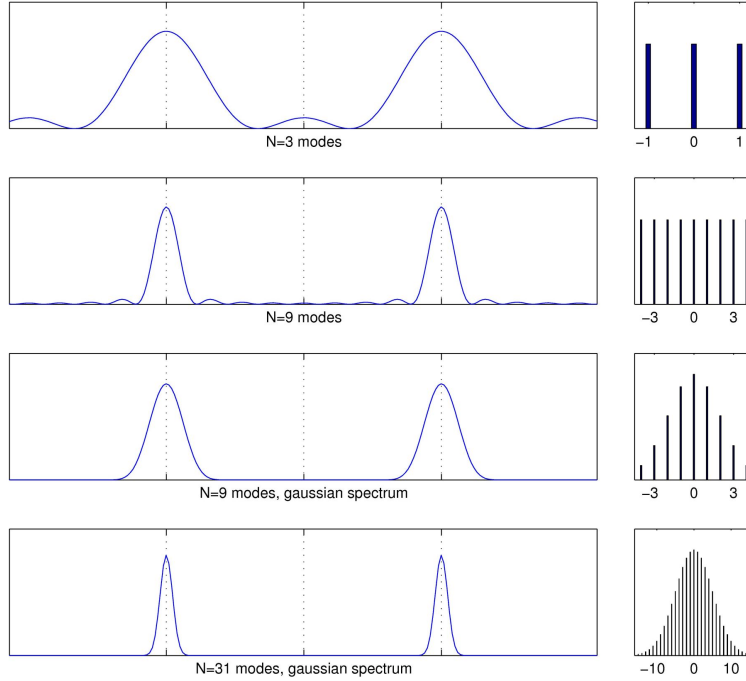


Figure 2.4: Shape of the pulses depending on the number of modes that are locked. You can also see how the side-maxima vanish, when the modes are modulated by a Gaussian. The widths of the Gaussian spectra are: $\sigma_9 = 2$ and $\sigma_{31} = 5$ respectively. The width of those pulses also depends on the width of the spectrum. The wider the spectrum, the smaller the pulse.

smaller constant:

$$I(t) = I_0 e^{-\frac{(4 \ln 2)t^2}{\tau^2}} \quad \rightarrow \quad \tau \cdot \Delta\nu = 0.441 \quad (2.5)$$

$$I(t) = I_0 \operatorname{sech}^2\left(\frac{t}{0.57\tau}\right) \quad \rightarrow \quad \tau \cdot \Delta\nu = 0.315 \quad (2.6)$$

With this you can calculate the minimum bandwidth for a given pulse duration. Assuming a sech^2 form and using $\Delta\nu = \frac{c}{\lambda^2} \Delta\lambda$ the values in Equation 2.5 are acquired. You can see that a very broad medium is needed for sub-10fs laser pulses.

Furthermore, if the intensity of the modes is modulated by a Gaussian profile as indicated in Figure 2.4, the side-maxima vanish. This situation very well describes the situation of a strongly inhomogeneously broadened laserline, like in Nd:glass for example [23].

τ	$\lambda = 800 \text{ nm}$	$\lambda = 1054 \text{ nm}$
1 ps	0.67 nm	1.17 nm
100 fs	6.7 nm	11.7 nm
10 fs	67 nm	117 nm
bandwidth $\Delta\lambda$		

Table 2.1: A few examples of the needed bandwidth for different pulse widths.

But how do you lock the modes in order to get an ultrashort pulse? Of course, there is a variety of techniques to do that. Acoustic loss modulation, is based on the diffraction of light by sound waves (Brillouin-scattering). Usually a piezo-driven quartz crystal is used to generate a sound wave that is timed such that the cavity loss is modulated at the mode frequency separation. Another way is using an electro-optical effect, where the refractive index is linear to an applied electric field. This method modulates the phase rather than the amplitude. More information about those two methods can be found in the popular lasers books such as [21] and [22]. Yet another way is using a saturable absorber.

2.3 Saturable Absorbers

Saturable absorbers have been used for modelocking practically ever since the solid state laser was invented [17, 24]. A saturable absorber can be described as a material that has decreasing absorbance with increasing intensities. Thus, to be in the most energy efficient state, the laser radiation tries to put all the energy into one position of the cavity. This leads to high intensities and short pulses. The width of the pulse is limited by many factors, such as the number of supported longitudinal modes and dispersion in intracavity devices. Saturable absorbers need to have the right wavelength range, should recover fast and have a saturation level suitable for intracavity intensities. There are different dyes that have this property. The problem is their toxicity and complicated handling. Furthermore, the upper state lifetimes of Ti:sapphire are significantly higher, while the cross section is much lower than in dye lasers. This will result in a poor gain saturation during one cavity roundtrip, making it hard to obtain mode-locking by means of a dye or active loss modulation. A faster absorber is needed. The next two sections will discuss semiconductor devices (SESAM) and Kerr-lens-modelocking (KLM) in more detail.

2.3.1 SESAM

Semiconductor saturable absorbers (SESAM) came up in the early 1990s and have significantly improved ever since [25, 26]. The basic principle behind it is the occupation of final states (in the conduction band) or depletion of the initial states (in the valence band) by photon transitions. Due to the advances in semiconductor engineering and growth technologies, they can be designed for a variety of applications. Their integration in mirrors make them very easy to handle. They have been used for picosecond to femtosecond pulses, Q-switching and CW-mode locking.

To understand their behavior a little more, let's have a look at the design

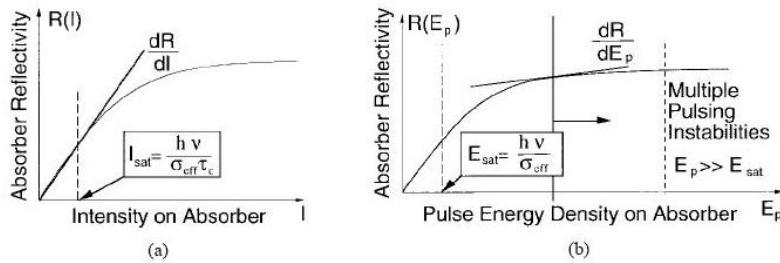


Figure 2.5: The change of reflectivity due to bleaching with the (a) CW intensity and (b) short pulses. [25]

criteria for a saturable absorber. Of course, the nonsaturable losses have to be kept to a minimum to maintain an efficient laser. Figure 2.5 shows a typical saturation behavior and it will help us understand the following. The time it takes to build up modelocking is inversely proportional to the slope at $I = 0$, as this will introduce a large change in reflectance for small intensity variations. Moreover to refrain from Q-switching, one has to respect the following condition derived in [27] and [28]:

$$\text{no Q-switching: } \left| \frac{dR}{dI} \right| I < r \frac{T_R}{\tau_2} \quad (2.7)$$

where R is the reflectance of the absorber, T_R the roundtrip time, τ_2 upper state lifetime of the laser and r the pump parameter, stating how much above threshold the laser is pumped [25]. The left side of this equation tells you how much more intensity is being reflected, i.e. the reduction of the losses due to the bleaching. While the right side determines the gain saturation per roundtrip. ‘If the gain cannot respond fast enough, the intensity continues to increase as the absorber is bleached, leading to self-Q-switching instabilities or stable Q-switching’ [25]. For fast absorbers, where the recovery time of

the absorber is much smaller than the cavity-roundtrip time ($T_A \ll T_R$), this condition is easily fulfilled. In order to take the small timescale of the pulses into account, another stability criterion has to be fulfilled to prevent Q-switched mode-locking, i.e. mode-locking that is modulated by a Q-switch envelope. Assume that the pulse length is shorter than the recovery time, $\tau_p < T_A$. The increase of reflection is now due to the bleaching by the ultrashort pulses, rather than the CW intensity. This is described by the fluence upon the saturable absorber, and gives us a condition given by [28]:

$$\text{no Q-switched mode-locking: } \left| \frac{dR}{dE_p} \right| E_p < r \frac{T_R}{\tau_2} \quad (2.8)$$

where E_p is fluence incident on the saturable absorber. This condition may be fulfilled by choosing $E_p \gg E_{sat}$. But experiments have shown that there is another effect, namely multiple pulsing, that comes into account for a high E_p [29]. For a high energy density E_p the reflection doesn't vary much anymore. And, as the gain for the broadband ultrashort pulses is limited by the laser material, two wider pulses with a smaller bandwidth, that see a higher average gain, are preferred. Setting E_p to about three to five times of E_{sat} is the rule of thumb to prevent multiple pulsing, given by the group of Prof. Ursula Keller at the ETH in Zürich. The incident pulse energy density can easily be varied by altering the size of the mode on the SESAM.

An inherently easier way to accomplish a saturable absorber, without using semiconductors, is the exploitation of the Kerr effect in a nonlinear medium.

2.3.2 KLM

Kerr lens modelocking was first discovered in 1990. The group of Ishida *et al.* and Sibbett's group both presented fs pulses that couldn't be described with the common mode-locking theories. There was no visible saturable absorber present in Sibbett's lasers [30], what lead to the term 'magic mode-locking'. It didn't take long for the first explanations of this phenomenon and many papers on this matter have been published [31–35]. The high intensities in the laser cavity will lead to nonlinear effects in the laser crystal. One of them being the 'Kerr effect'ⁱⁱⁱ. The refractive index is a function of the intensity:

$$n = n_1 + n_2 I(r, t) \quad (2.9)$$

The origin of this nonlinearity is related to the nonlinear polarization as discussed in Appendix B. Here the optical beam itself is strong enough to

ⁱⁱⁱnamed after the Scottish physicist John Kerr (1824-1907)

introduce such a nonlinearity. In combination with a Gaussian shaped pulse, this leads to a higher refractive index in the middle and a lower on the flanks of the pulse. Just like in a normal lens, the optical path is now longer at the center of the pulse, resulting in a focusing beam. This alone doesn't make a saturable absorber. In order to favor the high intensity an aperture is build into the resonator as seen in Figure 2.6. The cw-mode will be partially blocked by the aperture, i.e. it's loss will be high, while the higher intensities don't 'see' the aperture. Besides putting an aperture in the cavity, one can also reduce the mode in the gain medium. This is called 'soft-aperture' KLM. The focused beam has a larger overlap and therefore a higher gain than the low-intensity beam, giving rise to the same pulse forming mechanisms.

Kerr lens modelocking is a very fast and broadband absorber. It is broader

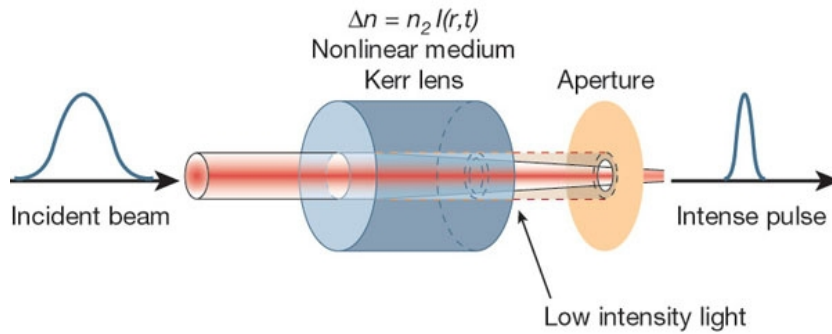


Figure 2.6: The principle of Kerr lens modelocking. The nonlinear refractive index n_2 in an intracavity material (usually the gain medium) focuses the intense beam. Low intensities are blocked by an aperture. [20]

than any other saturable absorber today. The high bandwidth makes broad wavelength tuning possible, which is used in many applications today. With only one laser, one can excite different autofluorescences in TPEM^{iv}, for example.

Unfortunately this technique has some considerable disadvantages. Because a quite high intensity is needed to make a considerable change in the mode size, KLM lasers are usually not self-starting. A brief perturbation, like vibrating one of the intra-cavity mirrors, is often used. This gives rise to some intensity fluctuations that will then start the pulse forming process. Furthermore, KLM works best close to the stability limit, as this leads to the biggest change in beam size. A correct alignment is therefore critical and sub millimeter accuracy is needed to establish ultrashort pulses. For a turn-key product, as used in this thesis, KLM by itself is therefore not a good

^{iv}Two Photon Excited Fluorescence Microscopy

option. Often a combination of these two methods is used to generate pulses, where the SESAM accounts for the starting of the pulse mechanism.

2.4 Propagation of Ultrashort Pulses

A more thorough description of the propagation of ultrashort pulses in dispersive media can be found in the books from Akhmanov [36] or Herrmann [37]. I will only introduce the main theoretical and experimental results in this section.

As mentioned above, a pulse is a superposition of many waves with small differences in the wavelength. Due to dispersion, every wave has a slightly different velocity. This phenomenon will lead to pulse broadening. Consider an electric field, such that:

$$E(z, t) = \frac{1}{2}A(z, t)e^{i(\omega_0 t - k_0 z)} + \text{c.c} \quad (2.10)$$

where $A(z, t)$ is the slowly varying envelope of the wave package, ω_0 the center frequency and $k_0 = \frac{n(\omega_0)}{c}\omega_0$ the wavenumber. Let's first find out the velocity of the pulse in the optical medium. The Fourier-Transform of Equation 2.10 yields:

$$\tilde{E}(z, \omega) = \tilde{A}(z, \Omega) \cdot e^{-ik_0 z} \quad (2.11)$$

where $\Omega = \omega - \omega_0$. The Fourier transform is used, as it provides a simple solution for the propagation in the z-direction:

$$\tilde{E}(z, \omega) = \tilde{E}(z=0, \Omega) \cdot e^{-ik(\omega)z} \quad (2.12)$$

This means for our assumptions from above, the solution is:

$$\tilde{A}(z, \omega) = \tilde{A}(z=0, \Omega) \cdot e^{-i(k(\omega) - k_0)z} \quad (2.13)$$

In most materials used in ultrafast optics it is safe to approximate the dispersion by a Taylor series expansion [38]:

$$\begin{aligned} k(\omega) &= k_0 + \left. \frac{dk}{d\omega} \right|_{\omega_0} (\omega - \omega_0) + \frac{1}{2} \left. \frac{d^2k}{d\omega^2} \right|_{\omega_0} (\omega - \omega_0)^2 + \\ &\quad + \frac{1}{3!} \left. \frac{d^3k}{d\omega^3} \right|_{\omega_0} (\omega - \omega_0)^3 + \dots \\ &= k_0 + k'\Omega + \frac{1}{2}k''\Omega^2 + \frac{1}{3!}k'''\Omega^3 + \dots \end{aligned} \quad (2.14)$$

With this assumption one can calculate the pulse envelope by simply plugging Equation 2.14 into Equation 2.13 and transform it back in to the time domain:

$$A(z, t) = \frac{1}{2\pi} \int d\Omega \tilde{A}(z=0, \Omega) \exp \left\{ i \left[(t - k'z)\Omega - \frac{1}{2}k''\Omega^2 - \dots \right] \right\} \quad (2.15)$$

If you stop after the linear term, you can see how the group velocity is defined:

$$A(z, t) = A(z=0, t - k'z) \Rightarrow v_g = \left. \frac{d\omega}{dk} \right|_{k_0} \quad (2.16)$$

The linear term will therefore account for the propagation of the wave package, but will not alter the shape of the pulse. Nevertheless, this approximation doesn't hold for an ultrashort pulse. As discussed earlier, a large bandwidth is needed to generate pulses in the fs regime. Therefore higher orders have to be taken into consideration when trying to build a resonator for ultrashort pulses. Let's first consider an expansion of $k(\omega)$ up to second order. The group velocity can than be written as:

$$\frac{1}{v_g(\omega)} = \left. \frac{dk}{d\omega} \right|_{\omega_0} = k'(\omega_0) + k''(\omega_0) \cdot (\omega - \omega_0) \quad (2.17)$$

this leads to (using another Taylor expansion)^v:

$$v_g(\omega) \stackrel{Taylor}{\cong} v_g(\omega_0) - k''(\omega_0)v_g^2(\omega_0) \cdot (\omega - \omega_0) \quad (2.18)$$

This shows that there is no well defined group velocity for a pulse. The fact that each spectral component has its own group velocity is called group velocity dispersion (GVD)^{vi}. $k'' = \left. \frac{d^2k}{d\omega} \right|_{\omega_0}$ is a measure for this quantity, with fs^2/m as its unit. For practical uses, the GVD of an optical element is expressed as:

$$D_2 = z \left. \frac{d^2k}{d\omega^2} \right|_{\omega_0} \quad (2.19)$$

In the visible range $k'' > 0$ for the commonly used materials in optics. According to Equation 2.18 the blue parts of the pulse will be slower than the

^v

$$\begin{aligned} v_g(\omega) &\cong v_g(\omega_0) + \left. \frac{dv_g(\omega)}{d\omega} \right|_{\omega=\omega_0} (\omega - \omega_0) = v_g(\omega_0) + \frac{k''(\omega_0)}{(k'(\omega_0) + k''(\omega_0)(\omega - \omega_0))^2} \Big|_{\omega=\omega_0} (\omega - \omega_0) \\ &= v_g(\omega_0) - k''(\omega_0)v_g^2(\omega_0) \cdot (\omega - \omega_0) \end{aligned}$$

^{vi}sometimes also called group delay dispersion (GDD)

red parts. This will not only lead to a broadening of the pulse, but also to a *chirp* of the pulse. The front of the pulse will be red and the back will blue. The effect on the pulse envelope will be briefly discussed in the following. Again, for a more detailed discussion I recommend the books mentioned earlier.

Using Equation 2.15 with a Gaussian pulse $A(t) = A_0 \exp(-\Gamma t^2)$, where Γ is complex and can even account for a chirp that had been introduced before entering the material of interest.

$$\Gamma = a + ib \quad (2.20)$$

The chirp is represented by b and the length of the pulse by a :

$$a = \frac{2 \ln 2}{\tau^2} \quad (2.21)$$

Tedious calculations finally lead to an intensity distribution:

$$I_{out}(z, t) = \frac{A_0^2}{4|\Gamma|\sqrt{\bar{a}^2 + t_2^2}} \exp \left\{ -\frac{\bar{a}t_1^2}{2(\bar{a}^2 + t_2^2)} \right\} \quad (2.22)$$

where I have defined:

$$\bar{a} = \frac{a}{4|\Gamma|^2}, \bar{b} = \frac{b}{4|\Gamma|^2}, t_1 = t - k'z \text{ and } t_2 = \bar{b} - \frac{1}{2}k''z$$

$I_{out}(z, t)$ is also a Gaussian, but the width has changed to be:

$$\tau_{out} = \tau_{in} \sqrt{1 + (2k''|\Gamma|)^2 z \left(z - \frac{b}{k''|\Gamma|^2} \right)} \quad (2.23)$$

what can now be simplified for an unchirped pulse ($b = 0$):

$$\tau_{out} = \tau_{in} \sqrt{1 + \left(\frac{4 \ln 2 k'' z}{\tau_{in}^2} \right)^2} \quad (2.24)$$

A quantity that is often being used in the lab to estimate the effects of a material on the pulse, is the propagation length z_D after which the width has doubled. From Equation 2.24 this yields to be:

$$z_D \approx 0.6 \frac{\tau_{in}^2}{k''}$$

When a 10 fs pulse propagates through Ti:sapphire ($k'' = 580 \text{ fs}^2/\text{cm}$) it only takes 1 mm to double the pulsewidth. Having this in mind, it seems that the second order approximation is still not good enough to describe fs-system. In fact, in ultrashort systems, such as the sub-two-cycle system from Morgner's group [19], third-order dispersion compensation is taken into consideration. But how can you compensate for GVD? Although all materials are having a positive k'' , there are still ways to compensate for this effect.

2.5 GVD Compensation

As I have just pointed out, the compensation of the GVD is very important in order to shorten the pulses. As usual, there is more than one way to go about that problem. The most common ones are the use of pairs of prisms or dispersive mirrors.

2.5.1 Prism Pairs

The use of prisms for negative dispersion was first introduced in the mid-eighties [39, 40]. While there will still be a positive GVD in the prism, the optical path will be longer for the red part. The arrangement is shown in Figure 2.7. The blue part is refracted at a higher angle than the red part and therefore hits the second prism more towards the top. This leads to a longer path for the red part in the second prism. After reflection at a plane mirror, the different spectral parts of the pulse are recombined. The red part is now trailing, thus the whole system introduces negative dispersion. The GVD can be linearly altered by the separation of the prisms, what makes it a very convenient setup to compensate for different GVDs.

By using Brewster cut prisms, the loss is quite low. The material that

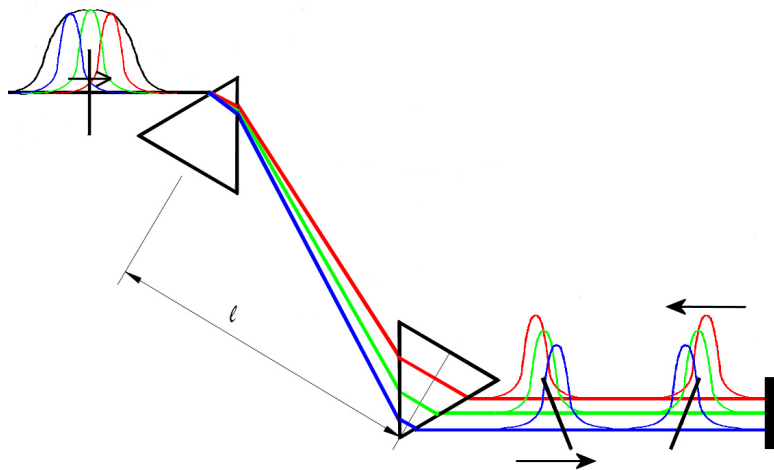


Figure 2.7: A prism pair setup to compensate group velocity dispersion in a resonator. [41]

is being used, should preferably have a low GVD itself to limit the second order dispersion. The beam should also be positioned on the very top of the

prisms, for the same reason. When choosing a prism material one shouldn't forget about the extra amount of third order dispersion that is introduced in the system. Sometimes it is better to use a prism material with lower GVD to keep the TOD down. By increasing the distance between the prisms the same effect is achieved as with a highly dispersive material. The obvious disadvantage of this system is the very delicate alignment of the prisms.

2.5.2 Dispersive Mirrors

A different method to compensate for GVD is the use of dispersive mirrors. Aligning a system with a dispersive mirror is quite insensitive, so that very stable systems can be set up. They came up in the mid-nineties and were first demonstrated on a KLM-Ti:Sapphire laser [42]. The mirrors are usually made of a stack of dielectrics. There are basically two different designs. The Gires-Tournois Interferometer (GTI) and chirped mirrors.

The dispersive effect in the GTI is obtained by making the duration each spectral component stays in the dielectric interferometer wavelength dependent. It is basically an etalon that has to be specially designed for each center wavelength. This is where the first problem comes in. The bandwidth is limited to half of the etalon-resonance spectrum, i.e. the part, with negative dispersion. It can therefore only be used for >20 fs pulses. Their low losses and ability to adjust the GVD by means of the entrance angle, still make them an option for systems with low gain and no need for shorter pulses.

The chirped mirror on the other hand doesn't use the duration but the penetration depth each component travels in the device to acquire dispersion. It is made of alternating layers (around 40) of highly and lowly refracting quarter waveplates. By using more than one mirror, a GVD of up to 50 fs^2 that is very flat over a large bandwidth can be achieved.

2.6 Self Phase Modulation

We have just discussed the consequences of the nonlinear refractive index n_2 in space (see Equation 2.9). It also has an effect in the time domain. The temporal distribution of the pulse leads to a time-dependent refractive index. With $\omega(t) = \frac{d\Phi}{dt}$ the instantaneous frequency will also shift. Assuming a Gaussian shaped pulse, you can easily determine the shift^{vii}:

$$\omega(t) = \omega_0 - \alpha \frac{2\pi}{\lambda_0} L \frac{d}{dt} n(I, t) \approx \omega_0 - \alpha n_2 t e^{-\left(\frac{t}{\tau}\right)^2} \quad (2.25)$$

^{vii}using: $n(t) = n_0 + n_2 I_0 e^{-\left(\frac{t}{\tau}\right)^2}$ and $\Phi = \omega_0 t - \frac{2\pi}{\lambda_0} n(I, t) L$

This is if we assume the pulse shape is not altered while passing the medium. This shows that only the change in intensity ($dn/dt \approx n_2 dI/dt$) is responsible for the change in frequency. For materials with $n_2 > 0$, as it usually is, the frequency of the rising part of the pulse will become lower but will increase for the trailing part.

For the center of the pulse ($t=0$) Equation 2.25 can be linearly approximated, using standard Taylor series expansion. A schematic graph for the intensity I , the introduced frequency shift $\Delta\omega$ and the resulting linearly chirped pulse are shown in Figure 2.8. Since the frequency broadening is symmetric around

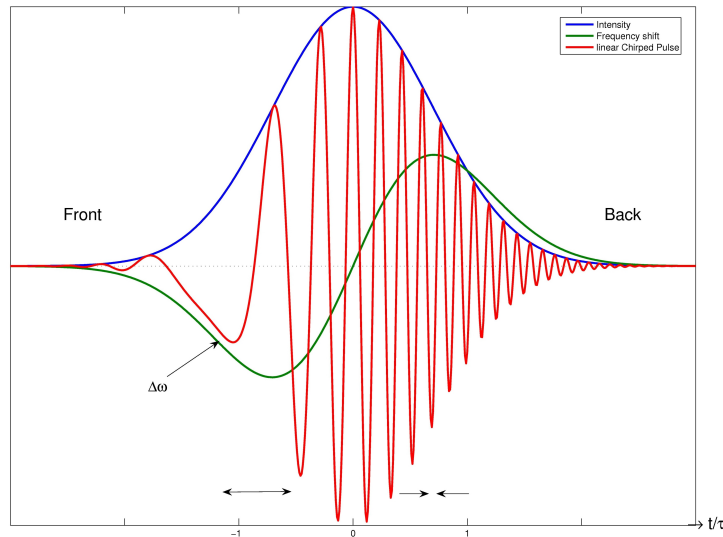


Figure 2.8: A simulation for a chirped pulse in a nonlinear medium. Note, that the chirp is a linear approximation of the shown frequency shift in the graph (green). Also, the front of the pulse is on the left and the back is on the right.

the mid-frequency, the pulse will not be broadened in the time domain. Nevertheless, in a normal dispersive medium, where the ‘redder’ portions of the pulse are faster, than the ‘blue’ ones, the pulse will be broadened in time, as the front of the pulse is faster, than the back. For a ‘anomalous’ dispersion ($k'' < 0$), e.g. a prism pair, the opposite is true and the pulse can even be compressed. Another modelocking-technique, called soliton-modelocking, also benefits from this effect [43]. Here, self-phase modulation and group velocity dispersion are in equilibrium, leading to a ‘soliton-like’ solution. This can explain, how a cavity with a saturable absorber, whose recovery time is in the order of a couple ps, can still produce fs-pulses.

Chapter 3

Fundus Microscopy

The first ophthalmoscope was introduced by Helmholtz in 1851. This instrument can image the light that is reflected by the fundus. The problem is that the retina is specifically built to absorb most of the incoming light. Thus only a small amount of light is reflected by the fundus, making it impossible to see the retina through a pupil without an optical device. The main obstacle for an observer is that he has to look from the same direction as an illuminating light source. Helmholtz' first ophthalmoscope consisted of a correcting lens and a semitransparent mirror that guided the illuminating light through the pupil into the eye. The reflected light can then be directly viewed through the semitransparent mirror (Figure 3.1). A historic review about Helmholtz' ophthalmoscope can be found in Ravin's article [44] that was published for the 150th anniversary of the invention.

Although this method only gives a qualitative description it was a major contribution to the diagnosis of many eye diseases. This was the first time doctors could look at the human retina. The upcoming of lasers and modern photon detection systems nowadays also allow for a quantitative description of the reflected light by the fundus and give more detailed insight.

In this thesis, the setup of a novel SLO that exploits the advantages of two-photon excited autofluorescence imaging and second harmonic generation is discussed. The two methods are explained in section 3.2 and should give an understanding of the principle physics behind it.

3.1 The cSLO

A confocal Laser Scanning Ophthalmoscope (cSLO) scans the retina in a raster-like fashion detecting the reflection from each individual pixel. A computer is used to form an image out of the individual intensity values for each

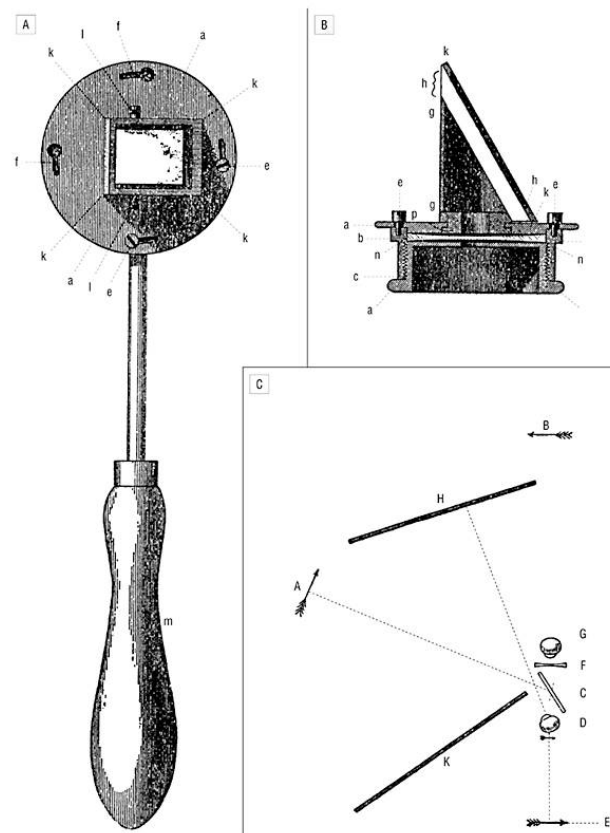


Figure 3.1: Drawing of an ophthalmoscope (from Helmholtz). A, Frontal view, facing patient. B, Vertical view, from superior surface looking downward. C, Depiction of path of light rays. [44]

pixel. The principle of confocal laser scanning was first described by Marvin Minsky at Harvard University in 1957. It has not had an impact until the upcoming of powerful laser light sources and better computers that are able to handle the massive amount of data. In 1979, finally, Brackenhoff [45] set up the first confocal microscope applying the theory derived by Sheppard [46] five years earlier.

The main principle of the confocal pinhole is shown in Figure 3.2. The laser is focused onto the specimen where it is either reflected or excites a fluorophore. The fluorescent light is usually collected through the same lens but then transmitted through a dichroic mirror. The confocal pinholes are in conjugate planes and make sure that only light from inside the focal region is collected. Light from outside is blocked by the aperture. The pinhole should be in the order of the FWHM of the Airy diffraction pattern generated by the first lens. This leads to a ‘pointlike’ illumination and detection. So this

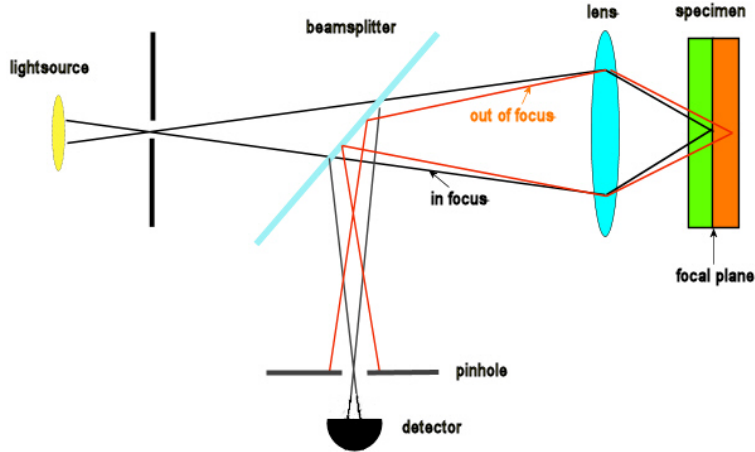


Figure 3.2: Setup of a confocal microscope

method has a big impact on the axial resolution that is enhanced by a factor $\sqrt{2}$. In order to get a 2D or 3D image the sample is raster-scanned, recording the intensity from each pixel (voxel). Using this information the image can be reconstructed with the help of a pc.

Although the explanation given above is very illustrative, to understand the process quantitatively geometric optics cannot account for that. Instead diffraction theory has to be used. Most of the following has been taken from the book by Bille and Schlegel [47]. The three dimensional intensity near the focus is given by:

$$I(u, v) = c \left| \tilde{h}(u, v) \right|^2 = C h(u, v) = C' \left| \int_0^1 J_0(v\rho) \exp\left(\frac{1}{2}iu\rho^2\right) \rho d\rho \right|^2 \quad (3.1)$$

where J_0 is the zero order Bessel function, $r = \sqrt{x^2 + y^2}$, C is a scaling constant, $\tilde{h}(u, v)$ is proportional to the electric field at the focus and u and v are related to the Cartesian coordinates by:

$$u = 8\pi n z \sin^2(\alpha/2)/\lambda \quad \text{and} \quad v = 2\pi n r \sin(\alpha)/\lambda$$

The optical coordinates u and v are often used to get rid of the dependency on the numerical aperture and the wavelength and therefore gives a more universal description. So far only the illumination is considered, $h(u, v)$ is

therefore also called the illumination point spread function (I-PSF). In fluorescence microscopy the I-PSF is directly proportional to the excitation of a fluorophore in the focus and consequently for the emission of a fluorescence photon at (u,v) . In a confocal microscope the detection path has to be taken into consideration as well. When using a confocal pinhole with a size of the first maximum, i.e. the FWHM of the Airy diffraction pattern, the detection probability is the same as the I-PSF, besides a correction for the different wavelength of the emitted light. This accounts for a factor $\varepsilon = \lambda_{\text{exc}}/\lambda_{\text{fl}} \approx 0.95$. In first order you can take ε as one and the resulting point-spread-function for the confocal microscope, C-PSF, can be written as:

$$h_{\text{conf}} = h_{\text{ill}}(u, v)h_{\text{det}}(u, v) \cong h^2(u, v) \quad (3.2)$$

By squaring the PSF the resolution is increased by a factor $\sqrt{2}$, as mentioned before. Additionally the fluorescence photons that arise out of focus get suppressed, which is an enhancement in axial resolution.

The first Laser Scanning Ophthalmoscope was introduced by Webb *et al.* [48] and has been improved ever since. In a cSLO the laser beam is shaped in such way that it focuses at the designated layer of the retina. It passes through an aperture or beamsplitter, which is used to distinguish between the illumination and the reflection. It gets deflected by a rotating polygon mirror to form a line scan. A two-dimensional scan is obtained by a galvanometric mirror, which deflects the beam vertically. The reflection of the eye travels back the same path, gets descanned by the two moving mirrors, before it reaches the photodetector. The signal is then fed into a frame-grabber, which displays the image on a computer screen. Today there are several commercial products that are used frequently in many eye clinics throughout the world and also in research facilities helping to get a better picture of the retina. The main advantages over the traditional fundus camera is the ability to distinguish between different layers, the large ratio of detection to illumination area and the absence of problems with chromatic aberrations. Furthermore the intensity of the illumination light can largely be reduced and it is therefore more comfortable for the patient. By using three different laser wavelengths one can even acquire a color image, which formerly could only be achieved with a fundus camera [49–51].

3.2 Non Linear Microscopy

The field of nonlinear microscopy only started with the arising of affordable high power lasers. It has now become available to a large group of researchers in many different sciences. But it had its biggest impact in the biosciences,

where it is now a widespread technique to image thick tissue and live animals. Several groups are working on nonlinear scanning laser ophthalmoscopes at the moment. Two photon excited (TPE) and second harmonic generation (SHG) imaging are of particular interest. The former, especially, is useful for the diagnosis of early stage AMD but has many other applications. An insight to these two techniques is given in the following two sections.

3.2.1 Two Photon Excited Microscopy

TPMEM uses the nonlinear excitation of a fluorescent by a multiphoton process. The theoretical basis for two photon events has been shown as early as 1931 by Maria Göppert-Mayer [52]. The first experiments with nonlinear two-photon excitation of a fluorescent had to wait for the invention of pulsed ruby lasers in 1960. It was demonstrated shortly after by Kaiser and Garret with $\text{CaF}_2:\text{Eu}^{3+}$ in 1961 [53]. It took another three decades for the first realization in a laser scanning microscope by Denk [11]. The basic principle

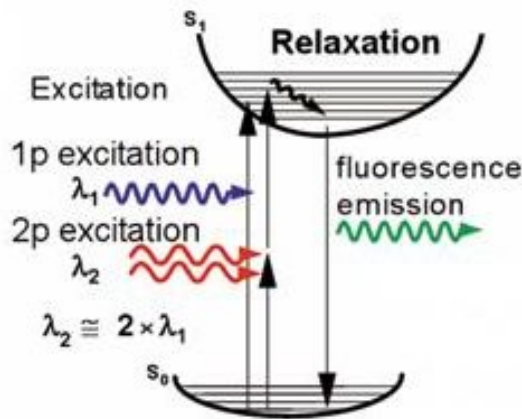


Figure 3.3: One photon absorption (blue) and two photon absorption (red)

www.nips.ac.jp

behind this approach is the use of two photons interacting with a molecule, producing an excitation equivalent to the absorption of a single photon possessing twice the energy [54] (see Figure 3.3). The first photon interacting with the molecule puts it in a so-called virtual state from which it can be excited into the existing state with the interaction of the second photon. The lifetime $\tau \sim 10^{-16}$ s of this virtual state can be estimated by Heisenberg's principle of uncertaintyⁱ. For a more detailed calculation one uses the appropriate order time-dependent perturbation theory [55], which shall not be

$$^i \Delta E \Delta t \approx \frac{\hbar}{2} \Rightarrow \Delta t \approx \frac{\lambda^2}{4\pi c \Delta \lambda} \approx 10^{-16} \text{ s}$$

discussed here.

The need for two photons makes this process nonlinear, i.e. there is a quadratic dependence on the intensity. The TPE processes have a much lower probability than the one photon absorption. Therefore two methods are combined to improve the photon output. By focusing, one increases the intensity at the focal spot, which leads to a higher TPE probability at focus with a rapidly vanishing probability outside. Furthermore, pulsed lasers are used to scan the specimen. This again leads to an increase in intensity, but keeps the average power relatively low. When using pulsed lasers, the fluorescence depends on the time-averaged square of the intensity

$$\langle I(t)^2 \rangle = \frac{g_p \langle I(t) \rangle^2}{R \tau} \quad (3.3)$$

where R is the number of pulses per second, τ is the FWHM of the pulse and g_p is a factor depending on the temporal shape of the pulse. This yields to an improvement of the TPE fluorescence by a factor of $\sim 10^5$.ⁱⁱ

As the wavelength is twice as long for TPE, the PSF for a two photon microscope looks like:

$$h_{\text{TPEM}} = h_{\text{ul}}^2 \left(\frac{u}{2}, \frac{v}{2} \right) \quad (3.4)$$

Due to the quadratic dependence there are two major advantages in comparison with ordinary cLSM. Photobleaching is only confined to the focal region rather than the whole axial direction in one photon excitation. In addition the dependence leads to an intrinsic optical sectioning effect and a confocal pinhole is therefore no longer requiredⁱⁱⁱ. This also gets rid of the problems with chromatic aberration in CLSM as well as the throughput losses, which arise from the blocking of scattered photons.

Looking at Abbe's limit it seems that the resolution using this method is worse by a factor two^{iv} compared with confocal laser scanning microscopy. But in practical use the resolution limit depends on many different factors. Such as the size of the pinhole, the number of collected photons, the ratio of true signal photons relative to scattered ones, and so on. Taking this into account and remembering that fluorescence only arises from the focal area (see Figure 3.4) the effective resolution using TPEM is often much better. Now, using twice the wavelength opens up a huge variety of fluorescents that are normally excited with UV light. This circumvents the use of UV optics,

ⁱⁱ $R = 80$ MHz, $\tau = 100$ fs and $g_p = 0.66$ for a Gaussian shaped pulse.

ⁱⁱⁱ Although it has also been shown that a confocal pinhole can increase both the lateral and the axial resolution under certain conditions [56].

^{iv} $d \geq \frac{\lambda}{2\text{NA}}$ where d is the lateral resolution, λ the illuminating wavelength and NA the Numerical aperture of the objective

makes the imaging less invasive for living tissue and also allows for much deeper scans.

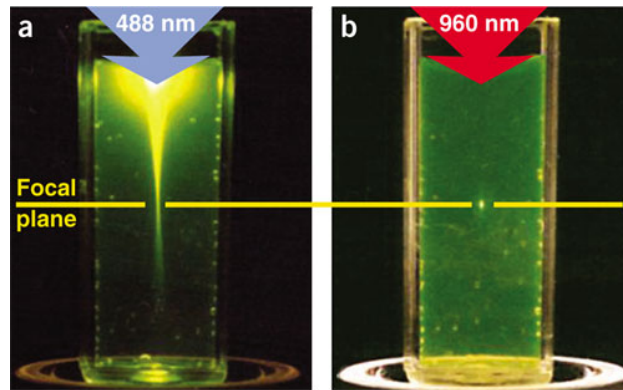


Figure 3.4: a) one photon absorption brings fluorescence from outside the focal area. b) confocal absorption only in the focus [54]

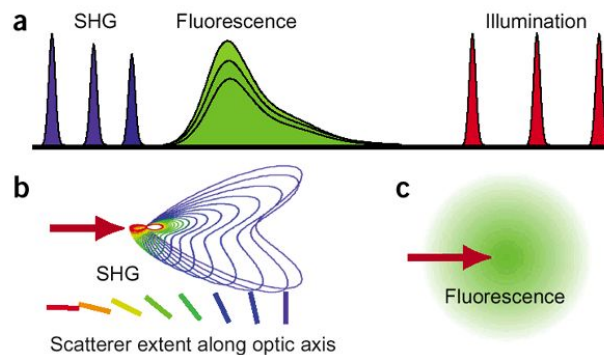


Figure 3.5: Two-photon fluorescence and SHG. (a) SHG is always at half the fundamental wavelength and tunes with the laser, whereas fluorescence emission is unchanged, except in its magnitude as the laser tunes through the TPE absorption peak. (b,c) SHG is directional depending on the distribution and orientation of the nonlinear dipoles (b), whereas fluorescence is, in general, isotropically emitted (c).[54]

3.2.2 SHG Microscopy

Second Harmonic Generation (SHG) imaging can be obtained with little modifications of the setup. SHG is a second order nonlinear process that has first been shown in 1961 by the group of Paul A. Franken [57] with a pulsed

ruby laser in a crystalline quartz sample. This is a nonlinear effect that can only be obtained in an anisotropic medium. It has been regularly used to frequency double lasers ever since. The first microscopic application was in 1974 by Hellwarth, where he examined the structure of polycrystalline ZnSe [58]. It took more than a decade for it to be applied on biological tissue by I. Freund *et al.* [59]. SHG comes from an induced second order polarization by an intense electric field (see Equation 3.5), i.e. the electric field of the laser itself.

$$P = \chi^{(2)} EE \quad (3.5)$$

This induced polarization leads to a production of a coherent wave with exactly twice the frequency. The wave is temporally synchronous with the incoming laser light unlike in TPEF where the temporal profile is determined by the lifetime of the fluorophore. The SHG signal is proportional to the second power of the peak intensity as stated in Equation 3.6,

$$I(2\omega) \propto \left(\chi^{(2)} \frac{P(w)}{\tau} \right)^2 \tau \quad (3.6)$$

where P is the pulse energy, τ the pulse width and $\chi^{(2)}$ the second order nonlinear susceptibility [60]. As $\chi^{(2)}$ is proportional to the density of the molecules with the nonlinear property, SHG depends quadratically to this density rather than linear as in TPEF. Another difference between those two imaging methods is the highly directed radiation of the SHG signal in contrast to the homogeneous emission of the TPEF signal. The directionality arises from phase matching constraints in this nonlinear process and leads to a dependency on the distribution and the directionality of the induced dipoles in the illuminated area [61, 62].

In Figure 3.5 some of the major differences are illustrated. Due to the very directional signal in SHG imaging that is mostly in the forward direction TPEF imaging is the method of choice for an in vivo ophthalmoscope.

Chapter 4

The Eye

4.1 Anatomy

This is only a short summary of the anatomy of the eye and is mainly based on references [63–66]. When looking in somebody’s face, you can see the pupil: a black looking aperture in the middle of the eye; the iris: a ciliary muscle that is in charge of the size of the pupil and has a distinctive color; and the sclera: the ‘white of the eye’ which is part of the supporting wall of the eyeball. In Figure 4.1 you can see a schematic drawing of the human eye. It can be divided into three layers:

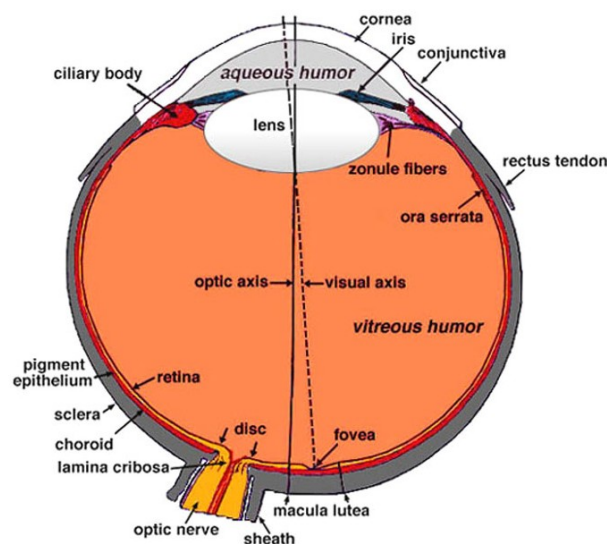


Figure 4.1: Sagittal horizontal section of the human eye. [63]

THE EXTERNAL LAYER: Which is divided in two sublayers the sclera in the rear part of the eyeball and the cornea where the light enters the eye. It is the most refractive part of the eye as will be discussed later (section 4.3).

THE INTERMEDIATE LAYER: Consisting of the choroid membrane, the iris and the ciliary body whose function is to accommodate and hold the lens.

THE INNER LAYER: Where the sensory part, the retina, resides. That's the place, where light gets absorbed by the different types of photoreceptors and converted into neural signals.

For light to be seen by a human being it passes through the transparent cornea and lens to be focused on the retina. The fovea is located in the center of the macula region of the retina as seen in Figure 4.1 and Figure 4.2. This tiny area (approximately 1.5mm of diameter) is responsible for our sharpest vision. It has the highest cone density [67] and the fewest layers of capillaries, to minimize the scattering of incident light. Another landmark of the retina is the optical nerve head. This is the area where the axons exit the eye to form the optical nerve. There are no photoreceptors in that area, leading to a 'blind spot'. You can just see it on the far right of Figure 4.2.

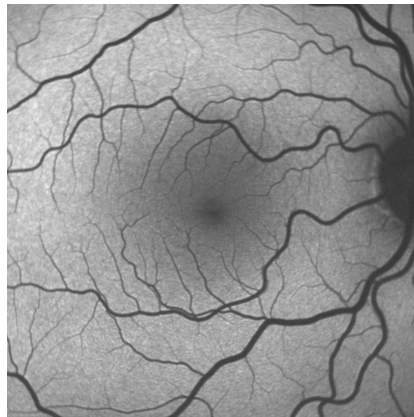


Figure 4.2: A picture of my retina taken with the HRA2 at the Moorfields Eye Hospital

4.2 Properties of the Retina

The retina (Figure 4.3) is approximately 500 μm thick and is made up of nerve cell bodies and two layers of synapses. It contains all of the sensory

receptors that convert the light into neural signals. It is therefore really a part of the brain. It sends all of this information through the optical nerve head to the visual cortex of our brain. Those nerves are made up of the axons of the ganglion cells, a type of neuron located at the innermost layer of the retina, i.e. the one closest to the lens. The inner part of the retina is made up of bipolar, horizontal and amacrine cells. The outer part of the retina is made up of cones and rods the actual photoreceptor cells. This means, that the light entering the eye has to travel through the whole thickness of the retina before activating the photoreceptors. The rods and cones are connected with the bipolar cells and horizontal cells in the outer plexiform layer. Furthermore the ganglion cells interact with the bipolar cells in the inner plexiform layer. But there are many other networks that altogether make up our vision. In cooperation with the visual cortex the retina takes care of color reception, detection of motion and distance, object recognition and many more aspects of vision.

When comparing different areas of the retina one can see that the retina

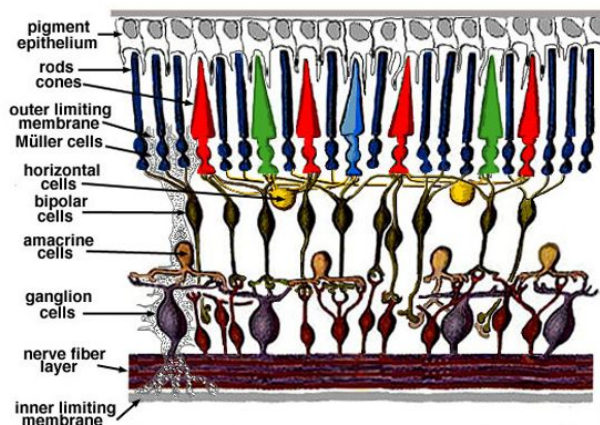


Figure 4.3: Diagram of the human retina. [63]

at the fovea is much thicker than at the peripheral fraction. This is due to the increased packing density of photoreceptors, particularly the cones and rods. The cones are mainly responsible for color vision. There are three different types of cones for three different colors as seen in Figure 4.4. They function best in daylight enabling us to see small visual details with great acuity. Cones also have a very fast response time making them able to perceive rapid changes. The rods on the other hand are for dimmer lighting conditions. They are very light sensitive, about 100 times more sensitive than cones. In addition to this, many rods connect to only one interneuron

resulting in a summation of the signals. This leads to a lower resolution but helps us detect movement in the retinal periphery.

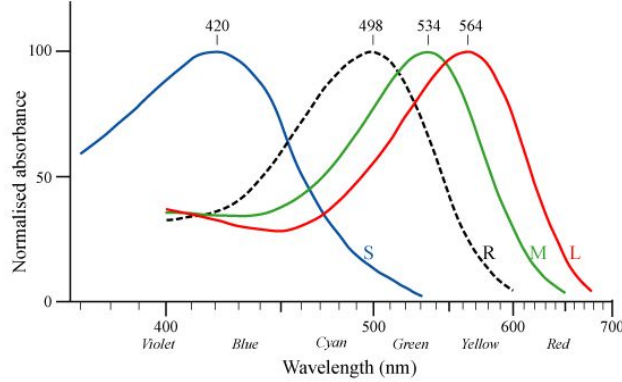


Figure 4.4: Normalized absorption spectra of human cone (S,M,L) and rod (R) cells [68]

4.3 The Optics of the Eye

The eye has been described as an optical instrument in many different ways. There have been many schematic eyes in the past. Some of the early examples are from Helmholtz (1866) and Gullstrand (1909). They differ only slightly and should not be considered a full description of the optical system of a human eye. As each eye has individual properties, the schematic eye represents the average eye. The Helmholtz and Gullstrand reduced schematic eyes both describe the cornea as one refracting surface and the lens as two. They use slightly different radii of curvature and refractive indices. I will describe two schematic eyes. The first only consisting of one refractive surface and the second being build up of four refractive surfaces. For the calculation I mainly use the following formulas.

$$D_{sum} = D_1 + D_2 - \frac{d}{n} D_1 D_2 \quad (4.1)$$

$$D_1 = \frac{n_1}{f_1} \quad \text{where} \quad f_1 = \frac{n_1 r}{n_2 - n_1} \quad (4.2)$$

Where Equation 4.1, known as the Gullstrand formula, describes the combined refractive power of two lenses separated by distance d in a medium with refractive power n and Equation 4.2 the refractive power of a sphere with radius of curvature r in a medium with n_1 in front of the sphere and n_2 behind.

4.3.1 The Reduced Eye

There is really not a lot to say about the reduced eye. It describes the human eye with one refractive surface, i.e. a lens. The focus of the lens is based on many clinical experiments and should describe an average healthy human eye. Of course, it lacks of precision, but for a principle understanding it is quite useful. Although the eye is 2.2 cm long, a focus length of 1.7 cm is used for this simple model, because there is no air in the eye. This corresponds to a refractive power of about 58.8 dpt

r_1	7.7	n_1	1	d_1	–
r_2	–6.8	n_2	1.376	d_2	0.5
r_3	10.0	n_3	1.336	d_3	–
r_4	7.911	n_4	1.386	d_4	0.546
r_5	–5.76	n_5	1.406	d_5	2.419
r_6	–6.0	n_6	1.386	d_6	0.635

Table 4.1: Properties of the normal eye - all length dimensions in mm

4.3.2 The Gullstrand-Le Grand Eye

This model describes the human eye as a more complex optical system. To calculate the total refractive power you need to know more about the refractive powers of the cornea and the lens. Gullstrand used a large number of normal eyes in order to evaluate the normal radii of curvature, distances and refractive indices. The cornea is treated as two surfaces with $r_{1,2}$ and d_1 as shown in Figure 4.5. It is a combined system of two lenses and with the values given in Table 4.1 we can calculate the refractive power of the anterior cornea surface:

$$D_1 = \frac{n_1}{f_1} = n_1 \frac{n_2 - n_1}{n_1 r_1} = 1 \frac{1.376 - 1}{7.7 \text{ mm}} = 48.83 \text{ dpt}$$

Of the posterior surface:

$$D_2 = \frac{n_3}{f_2} = n_3 \frac{n_3 - n_2}{n_3 r_2} = 1.336 \frac{1.336 - 1.376}{-6.8 \text{ mm}} = -5.88 \text{ dpt}$$

And thus the total refraction power D_{cornea} is, using Equation 4.1:

$$D_{cornea} = D_1 + D_2 - \frac{d}{n_3} D_1 D_2 = 48.83 \text{ dpt} - 5.88 \text{ dpt} + \frac{500 \text{ } \mu\text{m}}{1.376} = 43.05 \text{ dpt}$$

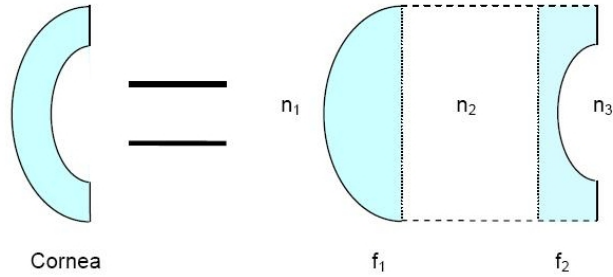


Figure 4.5: The cornea

The lens of the eye is biconvex and acts a converging lens. It is not homogeneous inside and is split into 4 areas to account for that. It can be looked at as a system of 4 lenses as demonstrated in Figure 4.6. As the inner part of the lens has a higher refractive index as the outer part, they all act as converging lenses. Calculations for the total refractive power are

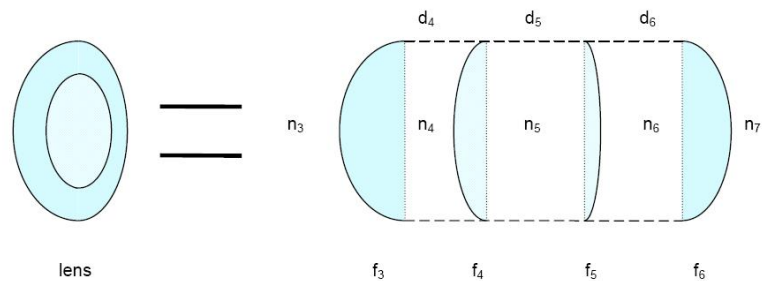


Figure 4.6: Simplification of the human lens

tedious as the distance d in the Gullstrand formula (Equation 4.1) has to be examined for each subsystem. With the values from Table 4.1 the total refractive power of the lens $D_{lens} = 19.11$ dpt. Using the Gullstrand formula one more time with $d = 5.7286$ mm and the refractive index of the aqueous humor $n = 1.336$ yields to a total refractive power of the eye:

$$D_{eye} = 58.64 \text{ dpt}$$

4.4 Ametropia

Ametropia is defined as an eye abnormality, such as nearsightedness, far-sightedness, or astigmatism, resulting from a faulty refractive ability of the eye. A large fraction of the population suffers from ametropia. The main reason for these errors results from an incorrect anatomy of the eyeball. To compensate for these aberrations, glasses, contact lenses or refractive surgery is used.

4.4.1 Hyperopia

Hyperopia, commonly referred to as far-sightedness, is an error of the eye leading to a focus that is behind the retina. Thus, the image looks blurred to the hyperopic person. Hyperopic people cannot focus on near objects and have to use some compensation in order to be able to read, for example. Usually a convex lens is used to make up for the decreased refractive power of the eye.

As one gets older, presbyopia will almost certainly affect ones vision. Presbyopia is a form of hyperopia. It is commonly believed that the lens reduces its elasticity, preventing it to deform as much as in younger years. The lack of deformation will result in a lower refractive power as can be readily verified with the formulas from the previous section.

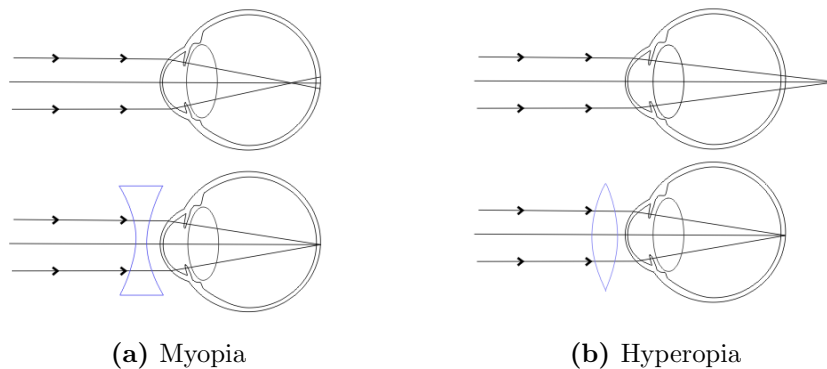


Figure 4.7: Ametropia: Both types of defocus and lenses that compensate for them

4.4.2 Myopia

Myopia is commonly known as short-sightedness. As the name suggests, distant objects cannot be focused by the myopic eye, making the image seem

blurred. The reason for not being able to focus correctly can be a long eyeball or a cornea with a small radius of curvature. Both result in the image being focused before the retina, as shown in Figure 4.7. This condition usually develops in childhood, during the time the eyeball grows. Sometimes the long-sightedness gained during the aging process may counteract the effects of mild myopia. Thus some people find that they can see without glasses again, when getting older.

To compensate for myopia, a converging lens is used, leading to a focus on the retina.

4.5 Fundus Reflectance

Soon after being able to quantify fundus images, models for the reflected light were proposed. The model used today is looking at the pathway of the light. It first passes the media until it hits the retina. After traveling through the many layers of the retina it finally hits the opaque white sclera. Light gets reflected whenever the refractive index changes between layers. In the following I will shortly describe each layer and its properties [69].

4.5.1 Reflectors of the Fundus

- **Cornea and lens**

The cornea and the lens account for most of the reflected light. It is tenfold higher than the reflection of the retina. This is due to the big change in the index of refraction. Most ophthalmoscopes circumvent this problem by separation of the entrance and the exit pupil. The confocal setup gets rid of it with the pinhole and the very small entrance pupil.

- **Nerve fiber layer**

The reflectance of the nerve fiber layer (NFL) reduces with decreasing thickness. It can therefore be neglected at the fovea. The cylindrical structure results in a strong directionality of the reflected light. The dependence on the thickness and the orientation make it hard to characterize.

- **Photoreceptors**

The cones are made of many discs. Each disc reflects a small part due to the change of the refractive index. Altogether this adds up to a measurable amount, which is assumed to be wavelength independent.

They are also orientated with their long axis pointing to the pupil. This high directionality allows the receptors to funnel the incoming light. It also leads to a reflectance that is bell-shaped over the location of the pupil plane, called the optical Stiles-Crawford effect.

- **Retinal Pigment Epithelium**

Many models suggest that some reflection also appears at the RPE. It is not quite sure from where exactly, but this idea has recently been strengthened by optical coherence tomography.

- **Sclera**

The sclera reflects about 50% of the incident light. All measurements found an increase in reflectance for increasing wavelength.

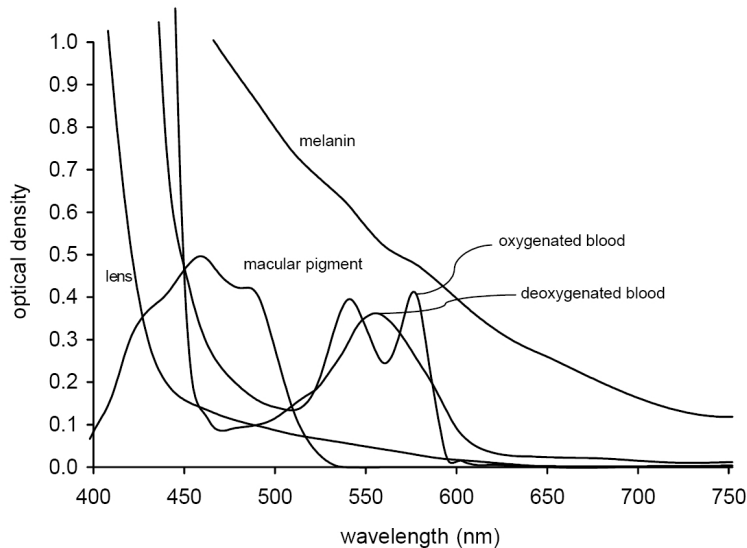


Figure 4.8: The absorption spectrum from different absorbers in the fundus taken from [69]

4.5.2 Absorbers of the Fundus

- **Ocular media**

The ocular media shows a strong dependence of the absorption on the wavelength. The lens strongly absorbs for $\lambda = 430$ nm with an increase in optical density over the age. Scattering will result in some losses as well. They can be treated wavelength independent. The vitreous doesn't absorb a lot, of course. It is usually treated like water with the only heavy absorption for $\lambda > 840$ nm.

- **Macular pigment** The macular pigment can be considered as a blue filter. It thereby possibly decreases photochemical light damage. It is located at the central area of the retina along the axons of the cones. Its spectral properties, absorbing between 390 nm and 540 nm make its thickness easily accessible.
- **Visual pigment** The absorbance of the cones and rods has been discussed previously. For completeness: there are three different types of cones with maximal absorbance at 420 nm, 534 nm and 564 nm, respectively. The maximum for the rods is at 498 nm. The optical density of the cones decreases with age, but it slightly increases for rods.
- **Lipofuscin** Lipofuscin is found in the basal part of the RPE and is connected to the phagocytosis of photoreceptors outer segments. It is made up of several fluorophores and A2E is supposed to play the major role. Altogether, lipofuscin absorbance decreases with increasing wavelength.
- **Melanin** You can find melanin in the choroid and the RPE. The optical density decreases monotonically for higher wavelengths.
- **Hemoglobin** There is a big difference between oxygenated and deoxygenated hemoglobin. While both types are almost transparent for $\lambda > 600$ nm, oxygenated blood has maxima at 416 nm, 542 nm and 577 nm and minima at 510 nm and 560 nm. On the other hand, deoxygenated hemoglobin shows a maximum at 559 nm and a minimum at 470 nm. The light is absorbed by the retinal blood vessels and also, but only very little, in the capillaries. The oxygen saturation in the choroidal blood is very high and commonly assumed to be 0.95.

4.6 Cataract

The clouding or yellowing of the lens is referred to as a cataract. It is the aging of the lens, which leads to a reduction of the transmission of light. Over 80% of people older than 75 years suffer from bad vision due to cataract. They have a blurred vision, especially in the dark. The name cataract, what actually means waterfall, describes their vision very well, which is even worse in low light levels. A cause of cataract is thought to be the decreasing blood supplement and therefore shortage of nutrition and oxygen [70].

The reduction of light is not uniform over the range of the visible spectrum. Blue light is affected more than the rest of the spectrum leading to a yellowish

lens [71].

As one can imagine, a cataract has substantial influence on the quality of images taken with an ophthalmoscope. Especially in diagnostic tools for the autofluorescence of the eye, blue laser light is used to excite the fluorophores. This results in a reduced recorded signal and makes the quantification more complicated. One way of getting around this problem is discussed in [72].

4.7 Age-related Macular Degeneration

Age-related macular degeneration (AMD) is the most common cause of severe visual loss in the Western world. Much effort has been put in to understand this disease better. A significant portion of the elderly is affected by this disease and a strong positive correlation with age has been shown in all studies. Broadly speaking, there are two types of AMD, referred to as *wet* and *dry*. Dry AMD occurs when the light-sensitive cells in the macula slowly break down. The breakdown leaves some cellular waste, known as drusen, at the RPE or Bruch's membrane, leading to a lack of nutrition for the cones and rods. This is thought to be caused by the reduced cell degradation capacity of the RPE cells. The drusen will lead to a detachment of Bruch's membrane from the RPE. Central Vision is gradually blurred in the affected eye. At first one can see a blurred spot in the center of their vision, gradually growing bigger over time. It is much more common than the wet type. About 85% of the AMD cases are related to the dry type, while the rest is connected to wet AMD. There is no treatment for dry AMD. All that can be done so far is to slow down the progress.

Wet AMD is progressing much faster and is caused by new blood vessels

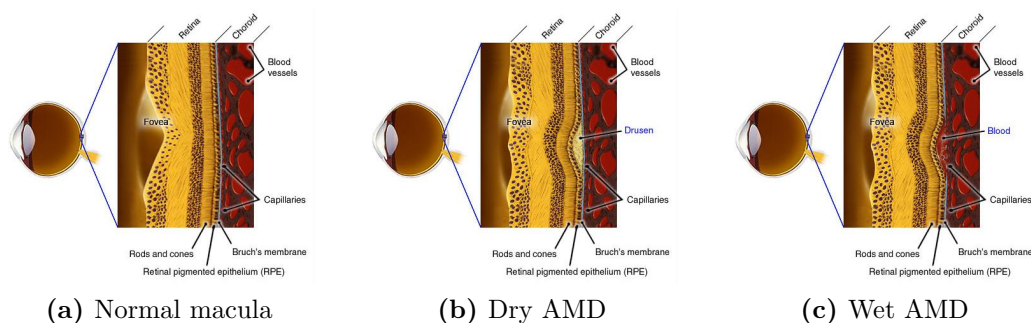


Figure 4.9: Comparison of the normal macula with dry and wet AMD. [73]

that grow between Bruch's membrane and the RPE. These new blood vessels are commonly very fragile and often leak blood and fluid. The blood and

fluid will raise the macula from its normal place, resulting in a fast progress of loss of vision. These vessels are built due to a common response of the body to the accumulated cellular waste. Usually it is a good thing that new vessels are being built to speed up the removal of the waste. But in this case it actually does more damage. Wet AMD can be treated by various approaches. They all try to get rid of the new vessels or at least prevent them from spreading. The most common treatments are laser coagulation and photodynamic therapy.

4.8 Lipofuscin

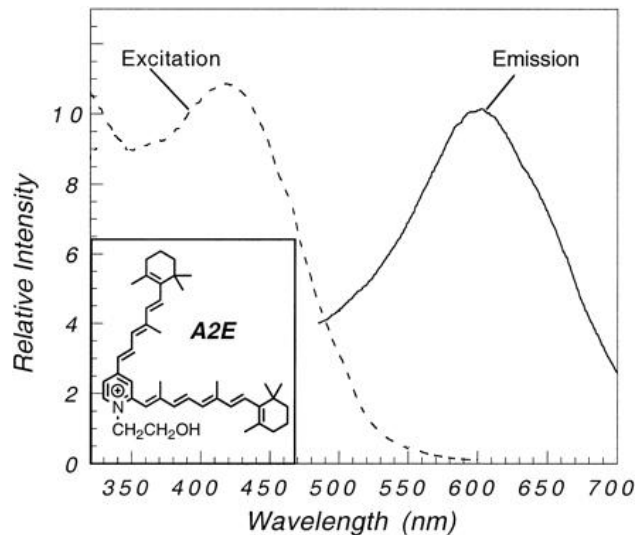


Figure 4.10: Excitation and emission spectra of A2E in methanol. The absorbance spectrum has a major peak at 435 nm and a smaller peak at 335 nm. The excitation spectrum, monitored at 600 nm emission, was similar in shape with a maximum at 418 nm. A 400 nm excitation wavelength generated a yellow emission centered around 602 nm. *Inset:* Structure of A2E. [3]

Lipofuscin is the fluorescent substance in the retina, which is mainly responsible for fundus autofluorescence [6]. More than 90% of the fluorophore is a byproduct of the visual cycle. This component cannot be degraded with enzymes and therefore accumulates in RPE cells [74, 75]. The main fluorescent constituent of lipofuscin is A2E with an excitation spectrum peaking in the blue (Figure 4.10, [3]). A schematic drawing of the visual cycle can

be seen in Figure 4.11. A2E biosynthesis begins in the photoreceptor outer

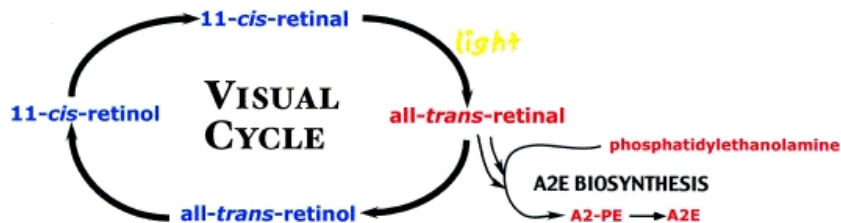


Figure 4.11: Visual Cycle and A2E formation [74]

segments when all-*trans*-retinal leaves the visual cycle. Rather than reducing to all-*trans*-retinol they react with phosphatidylethanolamine to form A2-PE. After phosphate hydrolysis A2E is being released. High levels of illumination seem to favor the formation of A2-PE and support the concept of a relationship between light exposure and deposition of A2E in RPE cells [74, 76]. Furthermore the amount of lipofuscin is an early indicator of retinal degradation and a relationship to AMD has been proposed in many papers [1, 4, 8]. The correct quantification of autofluorescence imaging is therefore of great interest in the understanding of retinal diseases.

Chapter 5

Results

5.1 Materials and Methods

This section describes the system that has been used. It shows what had to be modified in a conventional scanning laser ophthalmoscope to be suitable for two-photon excited fluorescence microscopy. A detailed graph of the setup and the most important facts about the system are presented. It also gives some details about the samples that have been imaged.

5.1.1 Optical Setup

A conventional scanning laser ophthalmoscope (Heidelberg Retina Tomograph (HRT), Heidelberg Engineering, Germany) had been modified for two-photon excited fluorescence microscopy by Olivier La Schiazza during his doctoral dissertation. The original fast resonant galvanometer scanning mirrors were used allowing a frame rate of 20 hertz, but the scan angle range was altered to allow for higher resolution optical ‘zooming’ at scan angles of $10^\circ \times 10^\circ$, $5^\circ \times 5^\circ$ and $1^\circ \times 1^\circ$. This results in a point-by-point excitation of a raster-scanned square on the specimen. A 1:3 Galilean telescope after the scanning mirrors adjusts the beam size at the back-aperture of the objective (U-V-I Apochromat, 40x/0.8 W, Leica) such that it is overfilled for a diffraction-limited focus on the sample. The specimen is mounted on a manual xyz-translation stage for proper positioning and focusing under the excitation beam.

In order to achieve the high intensities that are needed to overcome the low two-photon excitation cross section, femtosecond lasers were used for the epi-illumination path. First a mode-locked Ti:Sa laser (Mira 900, Coherent, USA) that was pumped by a DPSS CW laser (Verdi V5, $\lambda = 532$ nm, Coherent, USA) with a pulse width of $\tau \approx 150$ fs, a repetition rate $R = 78$ MHz

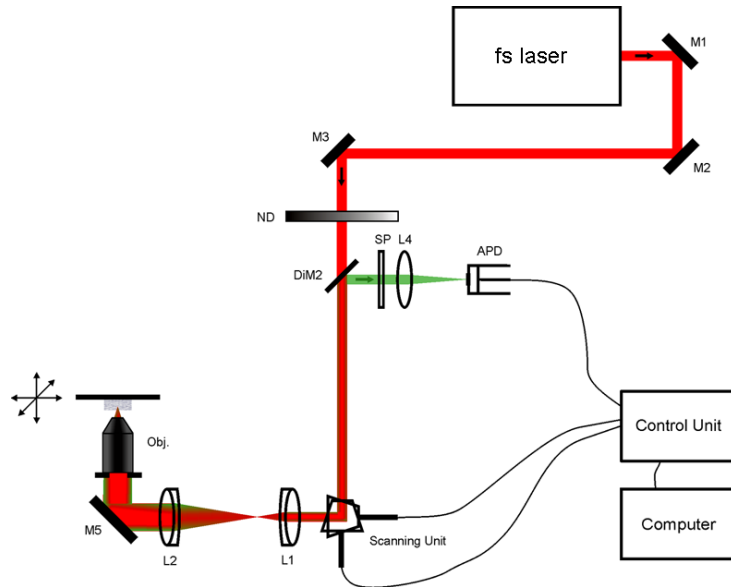


Figure 5.1: Optical diagram for a high-speed two-photon ophthalmoscope based on a conventional cSLO. Main components: fs laser, neutral density filter wheel ND, dichroic mirror DiM (Semrock), scanning unit HRT (Heidelberg Engineering), scan lens L1, tube lens L2, objective OBJ (40x/0.8 W, Leica), shortpass filter SP Semrock, avalanche photodiode APD. The APD is synchronized to the scanner through the control unit (HRT, Heidelberg Engineering) to construct a digital image from fluorescence intensity measurements at each pixel. The excitation light path is marked in red and the emission light path can be seen in green. [77]

and a wavelength tunable from 700 nm to 980 nm. Secondly a compact, all diode-pumped, solid-state Nd:glass femtosecond oscillator (*femtoTRAIN*TM Nd-Glas V1.0, High Q Laser, Austria) with a pulse width of $\tau \approx 250$ fs and a repetition rate $R = 75$ MHz. The power of the laser beam can be linearly adjusted by rotating a reflective neutral density filter wheel to prevent the sample from being ‘bleached’.

The detection path is basically the same as the excitation path. The fluorescent light is collected by the objective and descanned. It is then focused onto an avalanche photodiode (APD) by means of a dichroic mirror that only reflects the fluorescence light (380 – 720 nm, Semrock). To make sure that none of the excitation light is projected on the APD an additional IR-cut filter (750 nm cut-off wavelength, OD > 6, Semrock) was used. The nonlinear process makes the use of the original confocal pinhole redundant. A frame-grabber card electronically synchronizes the APD signal to the scanner to temporally and spatially reconstruct a digital 8-bit gray scale image (256 x

256 pixels). An average over 32 frames is taken to reduce the signal to noise ratio and the pixel dwell time is 0.25 μs . The field of view is (430x430) μm , (215x215) μm and (43x43) μm for the 10°, 5° and 1° scanning angles, respectively. A schematic diagram of the complete setup can be seen in Figure 5.1.

5.1.2 Sample Preparation

The human retinas were obtained from postmortem donor eyes from the Institute of Ophthalmology, University of Bonn, Germany. All from Caucasian donors with normal vision. After the anterior segment was removed for cornea transplantation, the posterior half of the eyeball was immediately fixed with paraformaldehyde (4% in phosphate-buffered saline (PBS), pH 7.4). There were no macroscopic visible retinal alterations such as retinal hemorrhage, or choroidal neovascularization [78, 79]. A 5 mm diameter retina/sclera probe from the macular and peripheral areas were prepared with a surgical trephine. The neurosensory retina was separated from the RPE-choroid-sclera complex. Specimens were transferred to a custom-made sample holder filled with a PBS (pH 7.4) solution and imaged with a large working distance water immersion objective, as discussed earlier.

5.2 Image Comparison

This section will compare the two different setups. The first subsection will talk about the different resolutions. In subsection 5.2.2 the power that is theoretically needed to achieve the same fluorescence output with both setups is compared to the experiment. Furthermore the fact that the image quality is similar to RPE images from a commercial slow-scanning two-photon microscope is discussed. The last part will talk about laser safety issues with the two laser systems.

5.2.1 Images From the Two-Photon Ophthalmoscope

The first images have been taken with the Ti:Sa laser as the illumination source. They are shown in Figure 5.2. The sample was illuminated with an average power of about 4 mW after the objective. Figure 5.3 shows the RPE cells imaged with the same setup but a Nd:glass oscillator for illumination. Here, a higher power of about 14 mW was needed for comparable brightness.

With both setups you can see that the autofluorescence is concentrated near the cell walls. Since the walls don't show any fluorescence, this makes it still

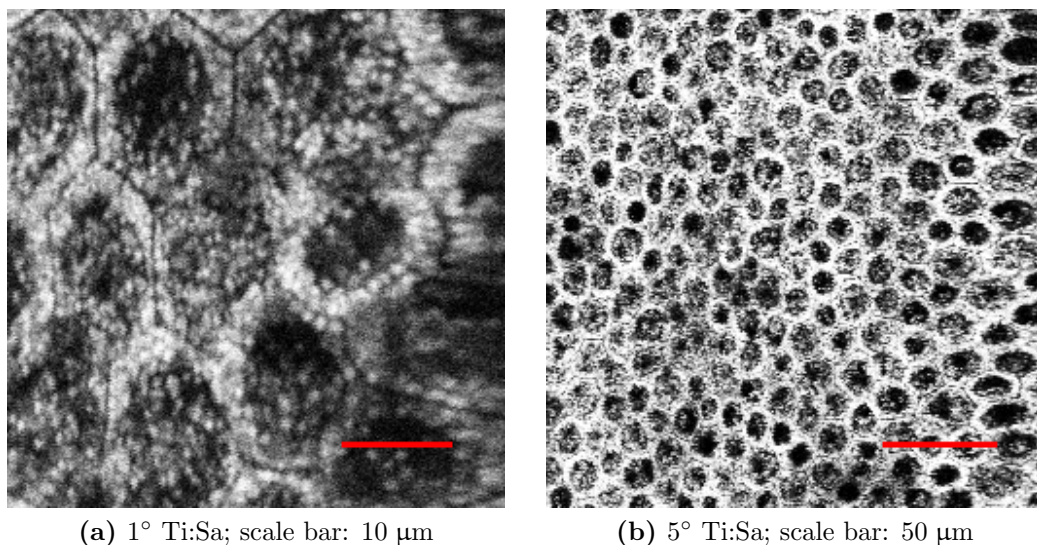


Figure 5.2: Two-photon excited autofluorescence images of RPE cells of a human donor eye in the macula region, through the high-speed two-photon ophthalmoscope and a Ti:Sa laser as a illumination source. Imaged with a power of $P = 4 \pm 1$ mW in front of the sample.

possible to figure out the shape of the cells. The RPE cells are of a hexagonal structure and are arranged in a very regular order, as seen in the 5° images. In the macula region they have a diameter of approximately 15 μm with the lipofuscin granules being clearly visible.

The resolution is slightly worse for the images taken with the longer wavelength. You cannot distinguish between single granules near the cell walls in Figure 5.3 but only the ones that are isolated in the center of the cells. The images acquired with the shorter wavelength show a better resolution and the single granules near the cell walls can also be discriminated from each other.

In theory, the lateral resolution is proportional to the wavelength and inversely proportional to the numerical aperture. Since two-photon excitation is proportional to the intensity square, the squared illumination point spread function (I-PSF²) is of interest. The 1/e radius of the I-PSF² can be estimated by fitting it to a Gaussian profile. For high numerical apertures ($NA > 0.7$) the 1/NA dependence deviates and can be approximated more precisely by an inverse power dependence [54]. The diffraction limited 1/e radius is given by:

$$\omega_{xy} = \frac{0.325 \lambda}{\sqrt{2} NA^{0.91}} \quad NA > 0.7 \quad (5.1)$$

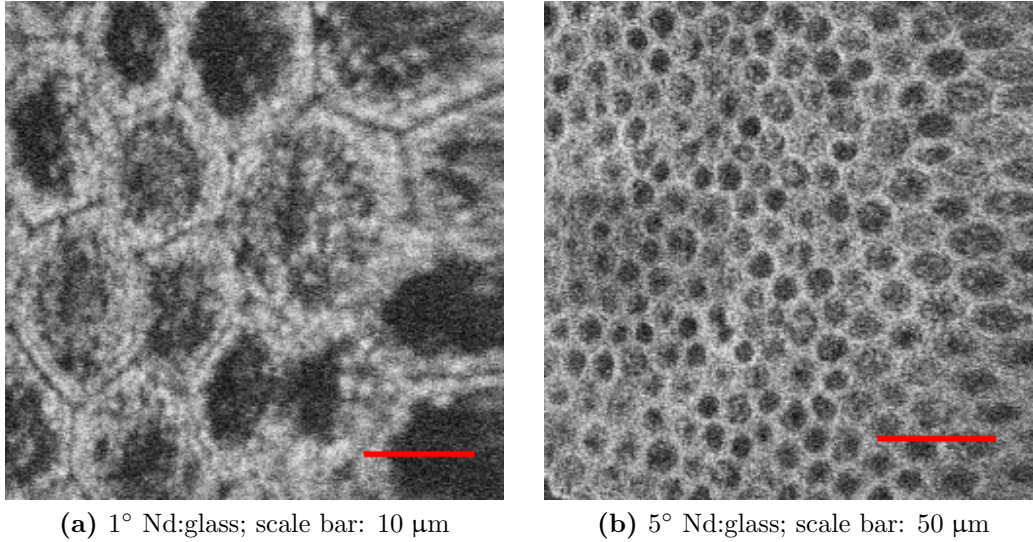


Figure 5.3: Two-photon excited autofluorescence images of RPE cells of a human donor eye in the macula region, through the high-speed two-photon ophthalmoscope with a Nd:glass laser for illumination. Imaged with a power of $P = 14 \pm 2$ mW in front of the sample.

To obtain the FWHM w_{xy} Equation 5.1 has to be multiplied with $2\sqrt{\ln 2}$. For the Ti:Sa setup with a numerical aperture $NA = 0.8$ the FWHM of the I-PSF² yields to be $w(\lambda = 830 \text{ nm}) = 0.39 \text{ μm}$ and for the Nd:glass $w(\lambda = 1054 \text{ nm}) = 0.49 \text{ μm}$. Since it is linear in the wavelength, the FWHM just differs by the factor $1054/830 = 1.27$.

To achieve a diffraction limited focus, the objective has to be overfilled. In practice this is accomplished if the $1/e$ beam radius is not smaller than the radius of the objective. This was true for the Ti:Sa laser, but the beam radius of the Nd:glass laser was slightly smaller. This also negatively affects the resolution leading to a slightly larger FWHM.

5.2.2 Comparing Fluorescence Efficiency

This section theoretically derives how much power is needed with a Nd:glass laser to achieve the same amount of fluorescence than with the Ti:Sa oscillator. The number of fluorescent photons is proportional to the time average of the square of the illumination intensity. From the original paper by Denk *et al.* [11] we know:

$$n_{\text{Fluor}} \propto \frac{P^2}{\tau R^2} \left(\frac{NA^2}{2\hbar c \lambda} \right)^2 k(\lambda) \quad (5.2)$$

where R is the repetition rate, τ the pulse width, λ the wavelength of the illumination light source and c the speed of light. The excitation cross-section of lipofuscin, as seen in Figure 4.10, also plays a role, which is taken into account by a dimensionless constant $k(\lambda)$.

The relative fluorescence yield ρ for our two systems can now be calculated:

$$\rho = \frac{n_{\text{Fluor}}(\text{Ti})}{n_{\text{Fluor}}(\text{Nd})} = \frac{\frac{P^2}{\tau R^2} \left(\frac{\text{NA}^2}{2\hbar c \lambda}\right)^2 k(\lambda) \Big|_{\text{Ti}}}{\frac{P^2}{\tau R^2} \left(\frac{\text{NA}^2}{2\hbar c \lambda}\right)^2 k(\lambda) \Big|_{\text{Nd}}} \quad (5.3)$$

As the same objective (U-V-I Apochromat, 40x/0.8 W, Leica) was used in both images this can be simplified to:

$$\rho = \frac{\frac{P^2 k(\lambda)}{R^2 \tau \lambda^2} \Big|_{\text{Ti}}}{\frac{P^2 k(\lambda)}{R^2 \tau \lambda^2} \Big|_{\text{Nd}}} \quad (5.4)$$

When taking the images obtained with the Ti:Sa laser as a reference, one can calculate the power that is needed with the Nd:glass laser to get the same number of fluorophores. With $k(830 \text{ nm})/k(1054 \text{ nm}) \approx 10/3$ and the numbers given in Table 5.1 we get:

$$P_{\text{Nd:glass}} = \sqrt{\frac{k_{\text{Ti}} R^2 \tau \lambda^2 \Big|_{\text{Nd}}}{k_{\text{Nd}} R^2 \tau \lambda^2 \Big|_{\text{Ti}}}} P_{\text{Ti:Sa}} \approx 2.9 P_{\text{Ti:Sa}} \quad (5.5)$$

This calculation is just a rough estimate, but it fits quite well with the

	Ti:Sa	Nd:glass
R[MHz]	78	75
τ [fs]	150	250
λ [nm]	830	1054
P[mW]	4 ± 1	14 ± 2

Table 5.1: Properties of the two different lasers as used during the experiments. Where R is the repetition rate, τ the pulsewidth, λ the wavelength and P the power on the sample.

experimental data.

$$P_{\text{Nd:glass}}/P_{\text{Ti:Sa}} = 14/4 = 3.5 \pm 1.0$$

Of course, this calculation leaves out many other influencing factors. The sensitivity of the photodiode was different for each image. It was manually adjusted to get a high contrast but limit overexposure. Other things that have not been considered are the wavelength dependency of the powermeter and different dispersion through the optical setup and therefore different temporal pulse broadening.

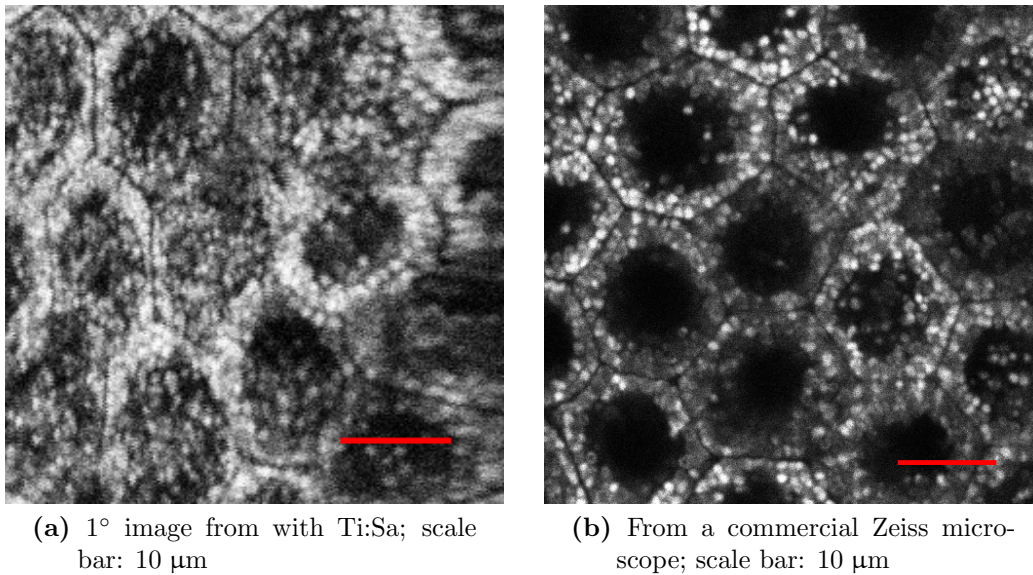


Figure 5.4: (a) The RPE cells taken with the high-speed Ophthalmoscope with the Ti:Sa laser used for illumination. (b) The RPE cells imaged with a slow-scanning two-photon microscope (Zeiss LSM 510 NLO).

5.2.3 Comparison With a Slow-scanning Microscope

Images of the RPE cells have also been taken with a commercial slow-scanning microscope (Zeiss LSM 510 NLO). The microscope also uses a Ti:Sa laser (Coherent Cameleon XR) and the power at the sample is about 4 mW. The scanning unit is much slower compared to the high-speed ophthalmoscope. The images taken with the Zeiss microscope had a pixel dwell time of about 400 $\mu\text{s}/\text{pixel}$, whereas the pixel dwell time in the ophthalmoscope is 0.25 $\mu\text{s}/\text{pixel}/\text{frame}$. Despite the different dwell times, the images from our fast-scanning ophthalmoscope are of similar quality than the ones from the microscope. Although image acquisition is similar with both machines, they are not comparable. The optical setup and the detection unit in particular are quite different. Nevertheless, it is surprising that a fast scanning device

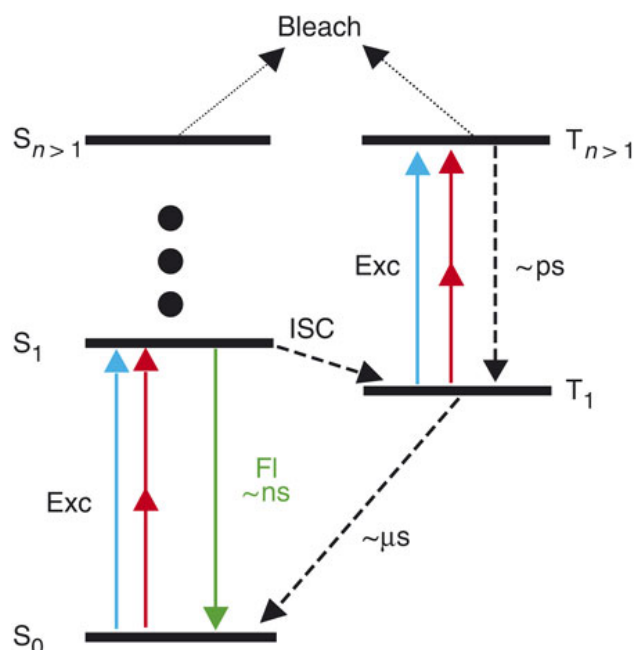


Figure 5.5: Energy diagram of a typical fluorophore. The major molecular pathways are shown: Excitation (Exc) -blue for single photon and red for two-photon absorption. Fluorescence (Fl) is shown in green. Intersystem crossing (ISC) and relaxation are drawn with dashed lines. The photo-bleaching pathway (Bleach) is also shown. S_0 , S_1 , $S_{n>1}$ are the singlet states, while T_1 , $T_{n>1}$ are the triplet states. [16]

collects a comparable amount of photons. The answer to this could lie in the photophysics of the fluorescent molecules. This has recently been proposed by Borlinghaus and Donnert *et al.* [15, 16]. The main idea is that in fast scanning fewer transient dark or triplet states are reached. The energy diagram of a typical fluorophore is shown in Figure 5.5. The molecule gets excited into a singlet state S_1 and has two options from there. It can either send out a photon (within a couple of ns) or can reach a triplet state T_1 through so called intersystem crossing. The excitation of T_1 is an effective bleaching pathway. With a lifetime of a few μs , excitation into a higher state and bleaching from there has a much higher probability in slow scanning mode than with high-speed scanning. Not only the total number of photons can therefore be comparable in both operation modes, but there are also fewer bleaching processes involved in fast-scanning.

To prove the mechanism discussed above, a lot more experiments have to be carried out that concentrate on the relation of scanning speed and fluorescence flux. First experiments are described in a paper by La Schiazza to be

λ [nm]	exposure time [s]	
	$< 10^{-11}$	$5 \cdot 10^{-5}$ -10
700 – 1050	$1.5 \cdot 10^{-4} C_4 C_6$	$18 \cdot t^{0.75} C_4 C_6$
1050 – 1400	$1.5 \cdot 10^{-3} C_4 C_6$	$90 \cdot t^{0.75} C_6 C_7$
maximum permissible exposure (MPE) [Jm^{-2}]		

Table 5.2: This table states the MPE for the human cornea according to VDE 0837 1:2001-11 for different exposure times. The constants are described in Table 5.3. [80]

published soon [14]. More on this will be investigated in the diploma thesis of Caroline Müllenbroich and Olivier La Schiazza’s doctoral thesis, both to be published early in 2008.

5.2.4 Laser Safety

Laser safety is, of course, a very delicate issue when talking about a diagnostic tool for clinical use. Since the eye will focus the light onto the very fragile retina, standards have to be fulfilled that ensure that the eye is not harmed. The use of a wavelength $\lambda > 1050$ nm has advantages over the Ti:Sa wavelength. The eye is nearly transparent there but still absorbs at $\lambda = 830$ nm, especially in the melanin. This leads to a favorable maximum permissible exposure (MPE) for the Nd:glass laser. Many experiments have to be made to find the correct MPE for all the different light sources. In Germany the industry standard DIN EN 60825 (VDE 0837 1:2001-11) regulates the MPE. Table 5.2 together with Table 5.3 gives an overview over the MPE for the wavelengths and exposure times of interest. After plugging in all the numbers, the MPE for $\lambda = 1054$ nm is about 27 times higher for a single pulse in the sub 10 ps region compared with $\lambda = 830$ nm. When imaging for more than 50 μs , i.e. when taking a whole set of 32 frames, one can use 14 times as much power with a Nd:glass laser. Considering the safety regulations, the higher power you need for the longer wavelength to obtain the same number of fluorescent photons doesn’t pose any threat. On the contrary, you can even yield a higher fluorescence flux by raising the power of the Nd:glass, while still staying below the MPE. This couldn’t experimentally be verified, since usual Nd:glass fs-lasers have output powers of about 150 mW. Our laser had a maximum average power of $P = 150$ mW, but after passing through the optical setup, only about $P = 18$ mW reached the sample. Higher powers can only be reached by pulse amplification, resulting in either a longer wave-

Parameter	Wavelength [nm]
$C_4 = 10^{0.002(\lambda-700)}$	700–1050
$C_4 = 5$	1050–1400
$C_6 = 1$ for $\alpha \leq \alpha_{\min}$	
$C_6 = \alpha/\alpha_{\min}$ for $\alpha_{\min} < \alpha \leq \alpha_{\max}$	400–1400
$C_6 = \alpha_{\min}/\alpha_{\max} = 66.7$ for $\alpha > \alpha_{\max}$	
$C_7 = 1$	700–1150

Table 5.3: Correction factors. $\alpha_{\min} = 1.5$ mrad and $\alpha_{\max} = 100$ mrad. α is the angle under which the beam diameter is seen by the observer. For a well collimated beam like in the SLO it can be assumed $\alpha < \alpha_{\min}$. [80]

length or a more complicated and therefore expensive setup with compression outside the resonator. Ti:Sa lasers, although being more expensive to begin with, have a higher output power. In addition they can be made tunable over a wide range with only few modifications. The best choice of laser will therefore vary from case to case.

Chapter 6

Summary and Discussion

Two femtosecond lasers for a nonlinear ophthalmoscope have been compared in this thesis. Both systems proved to be suitable for high resolution imaging of the RPE cells *ex vivo*. The lipofuscin is visible and also the shape of the cells can be determined. Although the Ti:Sa laser produced images of a higher resolution than the Nd:glass laser, for *in vivo* imaging this advantage will be less critical. First, according to DIN EN 60825 higher powers are applicable with the longer wavelength. This will result in more fluorescence, even though the lipofuscin is excited less. In addition, there will be less scattering within the eye, especially in the neurosensory part. This will lead to a better illumination of the retina. More fluorophores will therefore be excited with the Nd:glass laser.

The power that is needed for both femtosecond oscillators is also compared. Since the Ti:Sa laser has slightly shorter pulses resulting in higher intensities and the fluorophores have a higher two-photon cross section for 830 nm you need more power with the Nd:glass laser. The higher power that is needed for 1054 nm is not necessarily so disadvantageous. Since there is a lack of absorbers for the higher wavelength, the human eye can be illuminated with higher powers. Calculations even suggest, that by only obeying the maximum permissible exposure (MPE), one can still reach a higher fluorescence output with Nd:glass. Nevertheless, Nd:glass fs lasers usually don't have more than 150 mW average output power. A lot of the power is lost after going through all the optics in the setup, leading to relatively small room far an increase of the peak power at the sample. With new developments in ultrafast laser, very reliable and compact fs laser systems can now be produced with pulse widths of $\tau < 100$ fs and a lot more powerⁱ.

ⁱThe *femtoTRAIN*TM IC-1045-3000 from HighQ Laser, for example, is a Ytterbium

The two-photon ophthalmoscope presented in this thesis has more clinical uses besides imaging of the RPE cells and changes in the accumulation of lipofuscin. These measurements are of particular interest in age-related macular degeneration (AMD) research. Additionally to TPEF microscopy, the setup is also suitable for second harmonic generation (SHG) imaging. Another application of SHG imaging in the eye is the visualization of lamina cribosa, a mesh-like tissue around the nerves that exit the eye in the optical nerve head. A correlation of the size of the mesh and the intraocular pressure has been recently proposed [81]. Intraocular pressure plays an important role in glaucoma and SHG imaging can be an additional tool for an early diagnosis. First experiments by Mikael Agopov and Lukas Lomb in our group showed, that more power is needed for SHG imaging. The Nd:glass laser was not suitable for these experiments and only the Ti:Sa laser with a higher power output could be used for imaging.

To push this research towards clinical use, it has to be altered for *in vivo* imaging. The speed of imaging as presented in the optical setup used for this thesis is a first step into this direction. It is very significant in clinical practice. Being able to image at video speed (20 Hz) limits the time patients have to stare into the uncomfortable light. The examination time is also shorter. But the most crucial improvement compared to slow-scanning machines is the ability to limit eye movements during the acquisition of one frame. It only lasts 32 ms and there are no considerable movements during this time.

In addition, high-speed scanning can also result in a higher fluorescence yield, by allowing transient triplet or dark states to relax between re-excitation. This will be investigated in the near future and results should be achieved soon.

For first experiments with an illumination through an eye ball, a closed loop adaptive optics system needs to be integrated in the setup, similar to the one described in Christina Schwarz' diploma thesis [82]. With this setup, one can compensate for the aberration in the eye, as mentioned earlier. This will give a focus that is closer to being diffraction limited, resulting in a tighter focus spot than without such a system. Consequently, more fluorophores will be excited, due to the higher intensity. The resolution will also be better. This will be the next step and a lot of effort is put into this by various research groups.

laser with $\lambda = 1045$ nm and an average output power of $P = 3$ W.

The fs laser system of choice will have to be decided from case to case. Each system has advantages and disadvantages. The price and convenient handling is a big advantage for compact diode pumped or fiber lasers. The quite expensive Ti:Sa lasers with their tunability and high powers are very versatile, but also very expensive and usually only operated by experienced personnel. They will therefore be more suitable for research institutes, while the compact lasers will have advantages in everyday clinical use.

Appendix A

Resonator Stability

A.1 Ray Matrix

In normal geometric optics, you can characterize a *ray* with two parameters. The lateral displacement $r(z)$ and the slope $r'(z) = dr/dz = \tan \theta \approx \sin \theta \approx \theta$ as seen in Figure A.1. Such rays are called paraxial rays and the approximation is valid for angles $< 5^\circ$ with an error $< 1\%$. For such small angles the transformation is linear in r and r' and can therefore be described with matrices, called ABCD matrices. With this notation you can easily calculate a ray propagating through a lens, a curved mirror, air, etc via a matrix formalism. You can also get a matrix for a more complicated setup of different optical devices by simply multiplying the corresponding matrices.

$$\begin{bmatrix} r_f \\ r'_f \end{bmatrix} = \begin{bmatrix} A & B \\ C & D \end{bmatrix}_2 \begin{bmatrix} A & B \\ C & D \end{bmatrix}_1 \begin{bmatrix} r_i \\ r'_i \end{bmatrix} = \begin{bmatrix} A & B \\ C & D \end{bmatrix}_{1 \times 2} \begin{bmatrix} r_i \\ r'_i \end{bmatrix} \quad (\text{A.1})$$

In section A.2 we will justify the use of paraxial rays in a cavity. For further details go to [21], [22] or [83].

Here are some examples of ABCD Matrices:

$$\begin{bmatrix} 1 & \frac{L}{n_0} \\ 0 & 1 \end{bmatrix} \quad \begin{bmatrix} 1 & 0 \\ 0 & \frac{n_1}{n_2} \end{bmatrix} \quad \begin{bmatrix} 1 & 0 \\ \frac{-1}{f} & 1 \end{bmatrix} \quad \begin{bmatrix} 1 & 0 \\ \frac{-2}{R} & 1 \end{bmatrix}$$

ray propagation dielectric interface lens curved mirror

A.2 Paraxial Wave Equation

This section is to provide the foundations of the ray approximation used in the previous chapter. For a complete description of a laser resonator one still

needs to solve Maxwell's equations. But for many uses a scalar treatment is adequate. Let us first have a look on the full wave equation in vacuum:

$$\nabla^2 E(\vec{r}, t) - \frac{1}{c^2} \frac{\partial^2}{\partial t^2} E(\vec{r}, t) = 0 \quad (\text{A.2})$$

If we put an oscillating field $E(\vec{r}, t) = \tilde{E} \exp(-i\omega t)$ in Equation A.2 we obtain the Helmholtz equation:

$$\nabla^2 E + \frac{\omega^2}{c^2} E = 0 \quad (\text{A.3})$$

We now say that E is basically a traveling wave in the z -direction, but with a transverse amplitude and phase variation, thus any given vector component looks like:

$$\tilde{E} \equiv u(x, y, z) e^{-ikz} \quad k = \frac{2\pi}{\lambda} \quad (\text{A.4})$$

The transverse profile will change slowly with propagation distance z due to absorption and/or diffraction effects. Note that the rapid phase variation has already been factored out. Considering that a laser beam is usually well collimated and propagates as a unidirectional wave, we can use the *paraxial approximation* saying that the variations of u and $\partial u / \partial z$ within a distance of a wavelength in the z direction are negligible, i.e.:

$$\left| \frac{\partial u}{\partial z} \right| \ll \left| \frac{\partial u}{\partial x} \right|, \left| \frac{\partial u}{\partial y} \right| \quad \text{and} \quad \left| \frac{\partial^2 u}{\partial z^2} \right| \ll k \left| \frac{\partial u}{\partial z} \right| \quad (\text{A.5})$$

This is the same as saying that only the rays near the optical axis are of interest. Taking the Ansatz Equation A.4, using the approximations from above and plugging it all into the Helmholtz equation we get:

$$\left(\frac{\partial^2}{\partial x^2} + \frac{\partial^2}{\partial y^2} + 2ik \frac{\partial}{\partial z} \right) u(x, y, z) = 0 \quad (\text{A.6})$$

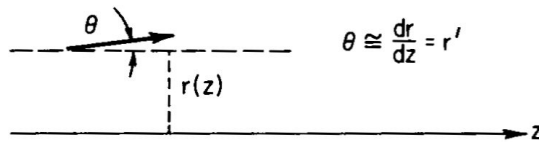


Figure A.1: A ray is characterized by the displacement and slope. [21]

which is known as the *paraxial wave equation*, and can also be written in the more commonly used form:

$$\nabla_t^2 + 2ik \frac{\partial}{\partial z} u(x, y, z) = 0 \quad (\text{A.7})$$

where $\nabla_t^2 \equiv \frac{\partial^2}{\partial x^2} + \frac{\partial^2}{\partial y^2}$. One important solution will be discussed in the next chapter.

A.3 Gaussian Beams

Consider a beam traveling along the z-axis. The intensity vanishes for points far away from the optical axis. A Gaussian beam intensity profile looks like:

$$I(x, y, z) \propto |u(\vec{r})|^2 e^{-2(x^2+y^2)/w^2} \quad (\text{A.8})$$

With the Ansatz:

$$u(\vec{r}) = A \exp\left(ik \frac{(x^2 + y^2)}{2q(z)}\right) \exp ip(z) \quad (\text{A.9})$$

where A is a constant and $q(z)$ and $p(z)$ are to be determined. Using the paraxial wave equation (A.7) we obtain a solution for $q(z)$, such that:

$$\boxed{\frac{1}{q(z)} = \frac{1}{R(z)} + \frac{i\lambda}{\pi w^2(z)}} \quad (\text{A.10})$$

where $R(z)$ is the radius of curvature, as seen in Figure A.2 and $w(z)$ is the spot size at any given point z. We choose the plane $z = 0$ to be that for which R is infinitely large and get the well known solutions for $R(z)$ and $w(z)$:

$$\boxed{R(z) = z + \frac{z_0^2}{z^2}} \quad \text{and} \quad \boxed{w(z) = w_0 \sqrt{1 + \frac{z^2}{z_0^2}}} \quad (\text{A.11})$$

where the *Rayleigh range* z_0 is defined as:

$$\boxed{z_0 = \frac{\pi w_0^2}{\lambda}} \quad (\text{A.12})$$

The Rayleigh range is the distance at which the beamwaist grows by a factor of $\sqrt{2}$, i.e. where the cross section area doubles. It therefore gives us a length

of a region at which the spot size w is smallest ⁱ.

From these formulas you can see that a Gaussian beam is fully characterized by the beam waist w_0 , the position of w_0 and the wavelength λ in the medium. With the results above and noting that

$$e^{ip(z)} = \frac{1}{\sqrt{1 + \frac{z_0^2}{z^2}}} e^{-i\phi(z)} \quad \text{where} \quad \phi(z) = \tan^{-1}(z/z_0) \quad (\text{A.13})$$

we can now write our solution of the paraxial wave equation as:

$$u(x, y, z) = \frac{A e^{-i\phi(z)}}{\sqrt{1 + \frac{z_0^2}{z^2}}} \exp\left(ik \frac{(x^2 + y^2)}{2R(z)}\right) \exp\left(-\frac{(x^2 + y^2)}{w^2(z)}\right) \quad (\text{A.14})$$

Equation A.14 describes a Gaussian beam, which is an exact solution to the paraxial wave equation (A.7). The intensity rapidly vanishes away from the z-axis, leading to an energy distribution that is concentrated in the beam. Moreover, the Gaussian beam remains a Gaussian beam as it propagates along the z-axis in vacuum. Only the parameters $R(z)$ and $w(z)$ have to be changed according to Equation A.11.

Another interesting point is the divergence of the beam. For distances $z \gg z_0$ the beamwaist asymptotically reaches a straight line as you can see in Figure A.2. With this in mind, a divergence angle θ can be defined:

$$\theta = \lim_{z \rightarrow \infty} \frac{w(z)}{z} = \frac{w_0}{z_0} = \frac{\lambda}{\pi w_0} \quad (\text{A.15})$$

From this equation you can see that a smaller beamwaist leads to a larger divergence angle and also a shorter Rayleigh range. It now shows that the properties of a Gaussian beam can be easily evaluated by the ABCD matrices used for ray optics in section A.1. Consider an initial beam q_i passing through an optical system described by an ABCD matrix. The q parameter q_f after passing this system is described according to

$$\boxed{q_f = \frac{A q_i + B}{C q_i + D}} \quad (\text{A.16})$$

The advantages of this law are obvious. One can now evaluate the transformation of a Gaussian beam by an optical system using the ray matrix of geometrical optics. By just knowing the matrix, you can predict the q parameter and therefore the beamwaist and the radius of curvature. This will help us evaluating different resonator designs and stability criterions of resonators in the next chapter.

ⁱalso compare to the f-number and the depth of field

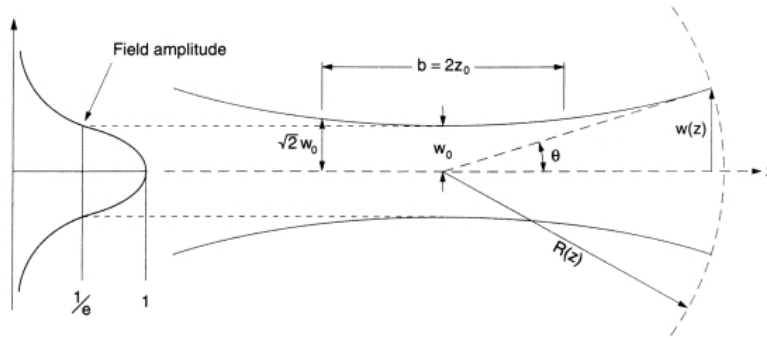


Figure A.2: Gaussian optics. [84]

A.4 Stable Resonators

With the help of Equation A.16 we are now able to describe a Gaussian beam propagating through any optical system. In this chapter this system will be a resonator.

Principle description

In a resonator we need a steady profile in order to have a stable setup. Just consider an imaginary plane in the resonator, which is perpendicular to the optical axis. A light field that passes this mirror will reach the mirror, be reflected, reach the mirror on the other side and is once more reflected before it reaches the plane again. If this field is to be a *mode* of the resonator, it must have exactly the same shape after one roundtrip. If this is a Gaussian beam we must have the same q parameter after one roundtrip, as before. This must be true regardless of the position of the imaginary plane, leading to

$$q(z) = \frac{A q(z) + B}{C q(z) + d} \quad (\text{A.17})$$

where z is anywhere within resonator.

Equation A.17 can be solved for $1/q$

$$\frac{1}{q(z)} = \frac{D - A}{2B} - \frac{i}{2B} \sqrt{4 - (A + D)^2} \quad (\text{A.18})$$

which directly leads to the radius of curvature (compare Equation A.10) and the beam waist in the reference plane.

$$\boxed{R = \frac{2B}{D - A}} \quad \text{and} \quad \boxed{w = \frac{\lambda}{\pi} \frac{2B}{\sqrt{4 - (A + D)^2}}} \quad (\text{A.19})$$

From this you can immediately see a necessary condition for the existence of a Gaussian mode, namely $(A + D)^2 > 4$.

A.5 Resonator Stability

For a simple resonator just take two curved mirrors. After one roundtrip the ray has to be transformed by the mirror to the left, a straight section of length L , the mirror to the right and another straight section with length L . In the matrix formalism introduced before, you just have to multiply the respective matrices to get the ABCD matrix describing the ray transformation by a roundtrip [21]:

$$\begin{aligned} \begin{bmatrix} A & B \\ C & D \end{bmatrix} &= \begin{bmatrix} 1 & 0 \\ -2/R_l & 1 \end{bmatrix} \begin{bmatrix} 1 & L \\ 0 & 1 \end{bmatrix} \begin{bmatrix} 1 & 0 \\ -2/R_r & 1 \end{bmatrix} \begin{bmatrix} 1 & L \\ 0 & 1 \end{bmatrix} \\ &= \begin{bmatrix} 1 - \frac{2L}{R_r} & 2L - \frac{2L^2}{R_r} \\ \frac{4L}{R_l R_r} - \frac{2}{R_l} - \frac{2}{R_r} & 1 - \frac{4L}{R_l} - \frac{2L}{R_r} + \frac{4L^2}{R_l R_r} \end{bmatrix} \end{aligned} \quad (\text{A.20})$$

To learn more about the cavity stability, we can now easily calculate the beam displacement and slope after N roundtrips.

$$\begin{bmatrix} r_N \\ r'_N \end{bmatrix} = \begin{bmatrix} A & B \\ C & D \end{bmatrix}^N \begin{bmatrix} r_i \\ r'_i \end{bmatrix} \quad (\text{A.21})$$

This equation can be solved with the help of ‘Sylvester’s Theorem’ as demonstrated in many standard textbooks, e.g. in [21]. The solution can be written as:

$$\begin{bmatrix} r_N \\ r'_N \end{bmatrix} = \frac{1}{\sin \theta} \begin{bmatrix} A \sin N\theta - \sin(N-1)\theta & B \sin N\theta \\ C \sin N\theta & D \sin N\theta - \sin(N-1)\theta \end{bmatrix}^N \begin{bmatrix} r_i \\ r'_i \end{bmatrix} \quad (\text{A.22})$$

where

$$\cos \theta = \frac{1}{2}(A + D) \stackrel{\text{Equation A.20}}{=} 1 - \frac{2L}{R_l} - \frac{2L}{R_r} + \frac{2L^2}{R_l R_r} \quad (\text{A.23})$$

from Equation A.23 and Equation A.22 you can see that θ has to be real for a stable resonator, which means $|\cos \theta| \leq 1$. This can be written as:

$$\boxed{0 \leq g_l g_r \leq 1} \quad (\text{A.24})$$

where g_l and g_r , the so called g parameters, are defined as follows

$$g_i = 1 - \frac{L}{R_i} \quad (\text{A.25})$$

Going back to Equation A.19 we see that this is exactly the same as the necessary condition $|A + D| < 2$ mentioned above.

Appendix B

Nonlinear Effects

B.1 Frequency Doubling

I will shortly introduce the theory behind frequency doubling. Starting out with the nonlinear polarization and susceptibility (section B.2) I will derive the wave equation and introduce the ‘non-depleted pump approximation’. Phase matching will be discussed in a very short manner. The interested reader should read the common literature for a deeper understanding.

B.2 Polarization and Susceptibility

The Polarization \vec{P} is the inner-electric field that arises from the distortion of the electron cloud, due to an external field. For weak external fields, the distortion can be approximated to be linear with the electric field. But for higher fields this no longer holds true and nonlinear effects have to be taken into consideration.

$$\begin{aligned}\vec{P} &= N \vec{p} \quad \text{N: Number of dipoles } \hat{=} \text{ valence electrons per volume} \\ &= q \vec{l} \\ &= q \left[\alpha^{(1)} \left(\frac{E}{E_a} \right) + \alpha^{(2)} \left(\frac{E}{E_a} \right)^2 + \dots \right] \frac{\vec{E}}{|E_a|}\end{aligned}\tag{B.1}$$

the polarization is normalized to a typical internal electric field E_a . The displacement of the electrons is in the order of $\alpha^i \approx d_a \approx 1$. Equation B.1 corresponds to a Taylor expansion in the electric field of the susceptibility. This model already gives a decent approximation for the refractive index. With

$$\vec{P} = \varepsilon_0 \chi^{(1)} \vec{E} + \vec{P}_{NL} = \varepsilon_0 \chi^{(1)} E + \chi^{(2)} E^2 + \dots$$

$$\chi^{(1)} = \frac{\vec{P}}{\varepsilon_0 E_a} = \frac{N_A e^- d_a}{\varepsilon_0 E_a} \Rightarrow n \approx 2.9$$

where $n^2 = \varepsilon = 1 + \chi^{(1)}$ and $E_a \approx \frac{e}{4\pi\varepsilon_0 d_a^2} \approx 1.4 \cdot 10^{-9} \frac{V}{m}$. This is not bad comparing it to a quartz with $n \approx 1.45$

B.3 Wave Equation

If one uses the nonlinear polarization, $\vec{P} = \varepsilon_0 \chi^{(1)} \vec{E} + \vec{P}_{NL}$, in the wave equation:

$$\Delta \vec{E} - \mu_0 \sigma \frac{\partial}{\partial t} \vec{E} - \mu_0 \varepsilon_0 \frac{\partial^2}{\partial t^2} \vec{E} = \mu_0 \frac{\partial^2}{\partial t^2} \vec{P}$$

it follows:

$$\Delta \vec{E} - \mu_0 \sigma \frac{\partial}{\partial t} \vec{E} - \mu_0 \varepsilon_0 \varepsilon_r \frac{\partial^2}{\partial t^2} \vec{E} = \mu_0 \frac{\partial^2}{\partial t^2} \vec{P}_{NL} \quad (\text{B.2})$$

where $\varepsilon_r = 1 + \chi^{(1)}$ and we assume that the linear dielectric susceptibility is frequency independent. By using the ‘slow varying envelope approximation’, Equation B.2 can be written as:

$$\frac{\partial}{\partial z} E(z, t') = -\alpha E(z, t') - \frac{1}{2} i \omega Z_w P_{NL}(z, t') \hat{e} \cdot \hat{p} e^{i(k-k_p)z} \quad (\text{B.3})$$

$$\alpha = \frac{\sigma Z_w}{2} \quad Z_w = \frac{1}{\varepsilon_0 \sqrt{\varepsilon_r} c} = \frac{\mu_0 n}{c} \quad t' = t - \frac{z}{c}$$

where \hat{e} is the direction of the electric field and \hat{p} of the polarization. This equation describes the change of the E-field over the length of the nonlinear medium. The conductivity σ of the medium leads to losses, whereas the nonlinear polarization can either amplify or dampen the field, depending on the relative phase of \vec{E} and \vec{P} . If the phase of the polarization is ahead by 90 deg it will pump energy into the field, and it will take energy in the opposite case. For $k \neq k_p$ phase matching will change over z as seen in the exponential.

B.4 Frequency Doubling

Frequency doubling was first demonstrated by Franken *et al.* in 1961 [57]. Here, the ‘non-depleted pump approximation’ is described, where only little energy from the fundamental wave is transferred to the higher harmonic and

thus it can be considered constant over the length of the nonlinear medium. Using:

$$P(2\omega) = \varepsilon_0 d_{\text{eff}}(2\omega : \omega, \omega) E(\omega, z) E(\omega, z)$$

put into Equation B.3 leads to:

$$\frac{\partial}{\partial z} E(2\omega) = -\frac{\omega}{n_{2\omega} c_0} d_{\text{eff}}(2\omega : \omega, \omega) E(\omega, z) E(\omega, z) e^{i[k(2\omega) - 2k(\omega)]z} \quad (\text{B.4})$$

This can now be solved with the assumptions discussed earlier:

$$E(2\omega, z) = -\frac{\omega d_{\text{eff}}}{n_{2\omega} c_0} E^2(\omega) \int_0^z dz e^{i\Delta k z}$$

So after going through a nonlinear crystal with length l :

$$E(2\omega, z) = -\frac{\omega d_{\text{eff}}}{n_{2\omega} c_0} E^2(\omega) \left(\frac{\sin \Delta k l / 2}{\Delta k l / 2} \right) e^{i\Delta k l / 2}$$

and from this we get the intensity:

$$I(2\omega, l) = \frac{2\omega^2 d_{\text{eff}}^2}{n_{2\omega} n_{\omega}^2 c^3 \varepsilon_0} l^2 I^2(\omega) \left(\frac{\sin \Delta k l / 2}{\Delta k l / 2} \right)^2 \quad (\text{B.5})$$

showing us that $I_{2\omega} \propto d_{\text{eff}}^2 l^2 I^2$ for $\Delta k = 0$ ⁱ. In case of no phasematching ($\Delta k \neq 0$), the induced polarization gets out of phase and will transfer energy back to the fundamental wave. The sinc-function has a coherence length $l_c = \frac{\pi}{\Delta k}$ in which the conversion of the fundamental to the frequency doubled wave is possible. This shows us, that it makes no sense using a crystal, that is longer as l_c .

ⁱThis is only true in the limits of our assumption: $I(2\omega) \ll I(\omega)$

Bibliography

- [1] Dorey, C., Wu, G., Ebenstein, D., Garsd, A. & Weiter, J. Cell loss in the aging retina. Relationship to lipofuscin accumulation and macular degeneration. *Invest. Ophthalmol. Vis. Sci.* **30**, 1691–1699 (1989).
- [2] Holz, F. *et al.* Inhibition of lysosomal degradative functions in RPE cells by a retinoid component of lipofuscin. *Invest. Ophthalmol. Vis. Sci.* **40**, 737–743 (1999).
- [3] Sparrow, J. R., Nakanishi, K. & Parish, C. A. The lipofuscin fluorophore A2E mediates blue light-induced damage to retinal pigmented epithelial cells. *Investigative Ophthalmology & Visual Science* **41**, 1981–1989 (2000).
- [4] Delori, F. C., Fleckner, M. R., Goger, D. G., Weiter, J. J. & Dorey, C. K. Autofluorescence distribution associated with drusen in age-related macular degeneration. *Invest. Ophthalmol. Vis. Sci.* **41**, 496–504 (2000).
- [5] Lois, N. *et al.* Fundus autofluorescence in patients with age-related macular degeneration and high risk of visual loss. *American Journal of Ophthalmology* **133**, 341–349 (2002).
- [6] Delori, F. *et al.* In vivo fluorescence of the ocular fundus exhibits retinal pigment epithelium lipofuscin characteristics. *Invest. Ophthalmol. Vis. Sci.* **36**, 718–729 (1995).
- [7] von Rückmann, A., Fitzke, F. W. & Bird, A. C. Distribution of fundus autofluorescence with a scanning laser ophthalmoscope. *Br J Ophthalmol* **79**, 407–412 (1995).
- [8] von Rückmann, A., Fitzke, F. & Bird, A. Fundus autofluorescence in age-related macular disease imaged with a laser scanning ophthalmoscope. *Invest. Ophthalmol. Vis. Sci.* **38**, 478–486 (1997).

- [9] Holz, F. G., Bellman, C., Staudt, S., Schutt, F. & Volcker, H. E. Fundus autofluorescence and development of geographic atrophy in age-related macular degeneration. *Invest. Ophthalmol. Vis. Sci.* **42**, 1051–1056 (2001).
- [10] Delori, F. C., Goger, D. G. & Dorey, C. K. Age-related accumulation and spatial distribution of lipofuscin in RPE of normal subjects. *Invest. Ophthalmol. Vis. Sci.* **42**, 1855–1866 (2001).
- [11] Denk, W., Strickler, J. & Webb, W. Two-photon laser scanning fluorescence microscopy. *Science* **248**, 73–76 (1990).
- [12] Squirrell, J. M., Wokonsin, D. L., White, J. G. & Baviste, B. D. Long-term two-photon fluorescence imaging of mammalian embryos without compromising viability. *Nature Biotechnology* **17**, 763–767 (1999).
- [13] Imanishi, Y., Batten, M. L., Piston, W., D. W. Baehr & Palczewski, K. Noninvasive two-photon imaging reveals retinyl ester storage structures in the eye. *Journal of Cellbiology* **164**, 373–383 (2004).
- [14] La Schiazza, O. & Bille, J. F. High-speed two-photon autofluorescence imaging of human RPE cells toward amd diagnostic. To be published.
- [15] Borlinghaus, R. T. Mrt letter: High speed scanning has the potential to increase fluorescence yield and to reduce photobleaching. *Microscopy Research and Technique* **69**, 689–692 (2006).
- [16] Donnert, G., Eggeling, C. & Hell, S. W. Major signal increase in fluorescence microscopy through dark-state relaxation. *Nat Meth* **4**, 81–86 (2007).
- [17] DeMaria, A., Stetser, D. & Heynau, H. Self mode-locking of lasers with saturable absorbers. *Appl. Phys. Lett.* **8**, 174–176 (1966).
- [18] Moulton, P. F. Spectroscopic and laser characteristics of $\text{Ti:Al}_2\text{O}_3$. *J. Opt. Soc. Am. B* **3**, 125–133 (1986).
- [19] Morgner, U. *et al.* Sub-two-cycle pulses from a Kerr-lens mode-locked Ti:sapphire laser. *Optics Letters* **24**, 411–413 (1999).
- [20] Keller, U. Recent developments in compact ultrafast lasers. *Nature* **424**, 831–838 (2003).
- [21] Milonni, P. W. & Eberly, J. H. *Lasers (Wiley Series in Pure and Applied Optics)* (Wiley-Interscience, 1988).

- [22] Siegman, A. *Lasers* (University Science Books, 1986).
- [23] Horvath, C. *Entwicklung von diodengepumpten Femtosekunden-Hochleistungs-Lasersystemen für die plasmainduzierte Ablation*. Ph.D. thesis, Ruprecht-Karls-Universität Heidelberg (1997).
- [24] Mocker, H. W. & Collins, R. Mode competition and self-locking effects in a q-switched ruby laser. *Appl. Phys. Lett.* **7**, 270–273 (1965).
- [25] Keller, U. *et al.* Semiconductor saturable absorber mirrors (sesams) for femtosecond to nanosecond pulse generation in solid-state lasers. *IEEE Journal of Selected Topics in Quantum Electronics* **2**, 435–453 (1996).
- [26] Sutter, D. *et al.* Semiconductor saturable-absorber mirror-assisted Kerr-lens mode-locked Ti:sapphire laser producing pulses in the two-cycle regime. *Optics Letters* **24**, 631–633 (1999).
- [27] Haus, H. Parameter ranges for cw passive mode locking. *Quantum Electronics, IEEE Journal of* **12**, 169–176 (1976).
- [28] Kärtner, F. X. *et al.* Control of solid state laser dynamics by semiconductor devices. *Opt. Eng* **34**, 2024–2036 (1995).
- [29] Aus der Au, J., Kopf, D., Morier-Genoud, F., Moser, M. & Keller, U. 60-fs pulses from a diode-pumped Nd:glass laser. *Optics Letters* **22**, 307–309 (1997).
- [30] Spence, D., Kean, P. N. & Sibbett, W. 60-fsec pulse generation from a self-mode-locked Ti:sapphire laser. *Optics Letters* **16**, 42–44 (1991).
- [31] Salin, F., Squier, J. & Piché, M. Mode locking of Ti:Al₂O₃ lasers and self-focusing: a Gaussian approximation. *Optics Letters* **16**, 1674–1676 (1991).
- [32] Cerullo, G., De Silvestri, S., Magni, V. & Pallaro, L. Resonators for Kerr-lens mode-locked femtosecond Ti:sapphire lasers. *Optics Letters* **19**, 807–809 (1994).
- [33] Haus, H. A., Fujimoto, J. G. & Ippen, E. P. Analytic theory of additive pulse and Kerr lens mode locking. *IEEE Journal of Quantum Electronics* **28**, 2086–2096 (1992).
- [34] Cerullo, G., De Silvestri, S. & Magni, V. Self-starting Kerr-lens mode locking of a Ti:sapphire laser. *Optics Letters* **19**, 1040–1042 (1994).

-
- [35] Herrmann, J. Theory of Kerr-lens mode locking: role of self-focusing and radially varying gain. *J. Opt. Soc. Am B* **11**, 489–512 (1994).
- [36] Akhmanov, S. A., Vysloukh, V. A. & Chirkin, A. S. *Optics of Femtosecond Laser Pulses* (AIP Press, 1992).
- [37] Diels, J.-C. & Rudolph, W. *Ultrashort Laser Pulse Phenomena, Second Edition (Optics and Photonics Series)* (Academic Press, 2006).
- [38] Fittinghoff, D. N. *et al.* Dispersion considerations in ultrafast cpa systems. *IEEE Journal of Selected Topics in Quantum Electronics* **4**, 430–440 (1998).
- [39] Fork, R., Mortinez, O. & Gordon, J. Negative dispersion using pairs of prisms. *Optics Letters* **9**, 150–152 (1984).
- [40] Gordon, J. & Fork, R. Optical resonator with negative dispersion. *Optics Letters* **9**, 153–155 (1984).
- [41] Kasper, A. *Erzeugung und Charakterisierung ultrakurzer Lichtpulse aus Titan:Saphir Laser Oszillatoren*. Ph.D. thesis, Max-Planck Institut für Quantenoptik (1998).
- [42] Szipocs, R., Ferencz, K., Spielmann, C. & Krausz, F. Chirped multilayer coatings for broadband dispersion control in femtosecond lasers. *Optics Letters* **19**, 201–203 (1994).
- [43] Kärtner, F. X., Jung, I. D. & Keller, U. Soliton mode-locking with saturable absorbers. *IEEE Journal of Selected Topics in Quantum Electronics* **2**, 540–556 (1996).
- [44] Ravin, J. G. Sesquicentennial of the ophthalmoscope. *Archives of Ophthalmology* **117**, 1634–1638 (1999).
- [45] Brakenhoff, G., Blom, P. & Barends, P. Confocal scanning light microscopy with high aperture immersion lenses. *Journ. of Microsc.* **117**, 219–232 (1979).
- [46] Sheppard, C. & Choudhury, A. Image formation in the scanning microscope. *Optica acta* **24**, 1051–1073 (1977).
- [47] Bille, J. & Schlegel, W. *Medizinische Physik* (Springer, 2005).
- [48] Webb, R. H., Hughes, G. W. & Delori, F. C. Confocal scanning laser ophthalmoscope. *Applied Optics* **26**, 1492–1499 (1987).

- [49] Manivannan, A., Kirkpatrick, J. N. P., Sharp, P. F. & Forrester, J. V. Novel approach towards colour imaging using a scanning laser ophthalmoscope. *Br J Ophthalmol* **82**, 342–345 (1998).
- [50] Reinholz, F., Ashman, R. A. & Eikelboom, R. H. Simultaneous three wavelength imaging with a scanning laser ophthalmoscope. *Cytometry* **37**, 165–170 (1999).
- [51] Fitzke, F. W. Colour imaging using a scanning laser ophthalmoscope. *Br J Ophthalmol* **82**, 337–338 (1998).
- [52] Göppert-Mayer, M. Über elementarakte mit zwei quantensprüngen. *Ann. Phys.* **9**, 274–294 (1931).
- [53] Kaiser, W. & Garrett, C. Two-photon excitation in $\text{CaF}_2:\text{Eu}^{2+}$. *Phys. Rev. Lett.* **7**, 612–614 (1961).
- [54] Zipfel, W., R.M. Williams, R. & Webb, W. Nonlinear magic: multiphoton microscopy in the biosciences. *Nature Biotechnol.* **21**, 1369–1377 (2003).
- [55] Faisal, F. *Theory of Multiphoton Processes* (Plenum, 1987).
- [56] Gauderon, R., Lukins, P. & Sheppard, J. Effect of a confocal pinhole in two-photon microscopy. *Microsc. Re. and Technol.* **47**, 210–214 (1999).
- [57] Franken, P., Hill, A., Peters, C. & Weinreich, G. Generation of optical harmonics. *Phys. Rev. Lett.* **7**, 118–119 (1961).
- [58] Hellwarth, R. & Christensen, P. Nonlinear optical microscopic examination of structure in polycrystalline ZnSe. *Opt. Commun.* **12**, 318–322 (1974).
- [59] Freund, I. & Deutsch, M. Second-harmonic microscopy of biological tissue. *Optics Letters* **11**, 91–96 (1986).
- [60] Campagnola, P. J., Clark, H. A., Mohler, W. A., Lewis, A. & Loew, L. M. Second-harmonic imaging microscopy of living cells. *Journal of Biomedical Optics* **6**, 277–286 (2001).
- [61] Moreaux, L., Sandre, O. & Mertz, J. Membrane imaging by second-harmonic generation microscopy. *J. Opt. Soc. Am. B* **17**, 1685–1694 (2000).

- [62] Mertz, J. & Moreaux, L. Second-harmonic generation by focused excitation of inhomogeneously distributed scatterers. *Opt. Commun.* **196**, 325–330 (2001).
- [63] Kolb, H., Fernandez, E. & Nelson, R. The organization of the retina and visual system (2006). URL <http://www.webvision.med.utah.edu>.
- [64] Silbernagl, S. & Despopoulos, A. *Taschenatlas der Physiologie* (Thieme, Stuttgart, 2003).
- [65] Schmidt, R. F., Lang, F. & Thews, G. *Physiologie des Menschen. Mit Pathophysiologie* (Springer, Berlin, 2004).
- [66] Lippert, H., Herbold, D. & Lippert-Burmester, W. *Anatomie. Text und Atlas* (Urban & Fischer Bei Elsevier, 2006).
- [67] Osterberg, G. Topography of the layer of rods and cones in the human retina. *Acta Ophthal.* **6**, 1–103 (1935).
- [68] Bowmaker, J. K. & Dartnall, H. J. Visual pigments of rods and cones in a human retina. *Journal of Physiology* **298**, 501–511 (1980). Image downloaded from Wikipedia on February 15th 2007.
- [69] Berendschot, T. T., DeLint, P. J. & van Norrena, D. Fundus reflectance-historical and present ideas. *Progress in Retinal and Eye Research* **22**, 171–200 (2003).
- [70] Schwingel, M. *Aspects of Dual Detector Ratio Imaging with a Scanning Laser Ophthalmoscope*. Master's thesis, Universitt Heidelberg (2006).
- [71] Mainster, M. A. & Sparrow, J. R. How much blue light should an IOL transmit? *Br. J. Ophthalmol.* **87**, 1523–1529 (2003).
- [72] Frank, F. *Autofluorescence imaging of the retina using a dual channel confocal scanning laser ophthalmoscope (cSLO)*. Master's thesis, Universität Heidelberg (2007).
- [73] About macular degeneration. American Health Assistance Foundation (2007). URL <http://www.ahaf.org/macular/about/maabout.htm>. Image downloaded on February 20th 2007.
- [74] Sparrow, J. R. *et al.* A2E, a byproduct of the visual cycle. *Vision Research* **43**, 2983–2990 (2003).

- [75] Katz, M. L., Gao, C.-L. & Rice, L. M. Formation of lipofuscin-like fluorophores by reaction of retinal with photoreceptor outer segments and liposomes. *Mechanisms of Ageing and Development* **92**, 159–174 (1996).
- [76] Saari, J. C., Garwin, G. G., Van Hooser, J. P. & Palczewski, K. Reduction of all-trans-retinal limits regeneration of visual pigment in mice. *Vision Research* **38**, 1325–1333 (1998).
- [77] La Schiazza, O., Agopov, M., Han, M. & Bille, J. Comparison of one-photon and two-photon excited autofluorescence of RPE cells from human donor eyes. In *ARVO Annual Meeting* (2007).
- [78] Bindewald-Wittich, A. *et al.* Two-photon-excited fluorescence imaging of human RPE cells with a femtosecond Ti:sapphire laser. *Investigative Ophthalmology & Visual Science* **47**, 4553–4557 (2006).
- [79] Han, M. *et al.* Two-photon excited autofluorescence imaging of human retinal pigment epithelial cells. *Journal of Biomedical Optics* **11**, 010501-1 – 3 (2006).
- [80] Sutter, E. *Schutz vor optischer Strahlung* (VDE Verlag GmbH, 2002).
- [81] Brown, D. J., Morishige, N., Neekhra, A., Minckler, D. S. & Jester, J. V. Application of second harmonic imaging microscopy to assess structural changes in optic nerve head structure *ex vivo*. *Journal of Biomedical Optics* **12**, 024029-1–5 (2007).
- [82] Schwarz, C. *Adaptive-optical correction of 1° images using a confocal Scanning Laser Ophthalmoscope*. Master's thesis, Ruprecht-Karls-Universität" at Heidelberg (2007).
- [83] Fowles, G. R. *Introduction for Modern Optics* (Dover Publications, 1989), 2 edn.
- [84] Efthimiopoulos, T. Laser. URL <http://ph1.physics.uoc.gr/enot1.2.gif>. Image downloaded on February 5th 2007.

List of Figures

2.1	Improvements in ultrashort pulse generation	4
2.2	Q-switching	5
2.3	The locking of 7 modes	6
2.4	Shape of the pulses depending on the number of modes that are locked	7
2.5	The change of reflectivity in SESAM	9
2.6	The principle of Kerr lens modelocking	11
2.7	Dispersion compensation with prism pair	15
2.8	Chirped pulse	17
3.1	Drawing of an ophthalmoscope	20
3.2	Setup of a confocal microscope	21
3.3	One photon and two photon absorption	23
3.4	One-photon vs two-photon excitation area	25
3.5	Two-photon fluorescence and SHG	25
4.1	Sagittal horizontal section of the human eye	27
4.2	HRA2 Image of the Retina	28
4.3	Diagram of the human retina	29
4.4	Normalized absorption spectra of human cone and rod cells . .	30
4.5	The cornea	32
4.6	Simplification of the human lens	32
4.7	Ametropia	33
4.8	The absorption spectrum from different absorbers in the fundus	35
4.9	Comparison of the normal macula with dry and wet AMD . .	37
4.10	Excitation and emission spectra of A2E in methanol	38
4.11	Visual Cycle and A2E formation	39
5.1	Optical setup of the ophthalmoscope	42
5.2	Images of the RPE cells with a Ti:Sa laser	44
5.3	Images of the RPE cells	45

5.4	RPE cells imaged with the Zeiss microscope	47
5.5	Energy diagram of a typical fluorophore	48
A.1	Characterization of a ray	56
A.2	Gaussian optics	59

Acknowledgments

Here I would like to express my gratitude to all those people who helped me in completing this diploma thesis.

My special thanks go to:

- Prof. Dr. Josef Bille for offering and supervising this thesis and his support throughout my work in his group.
- Prof. Dr. Christoph Cremer for his willingness to take on the second referee.
- Olivier La Schiazza and Mikael Agopov for their kind help in every aspect of this thesis. In particular for their help with the nonlinear ophthalmoscope.
- All members of group F1 for creating a nice atmosphere, a good working environment and helping me in and outside of the lab.

Erklärung:

Ich versichere, dass ich diese Arbeit selbstständig verfasst und keine anderen als die angegebenen Quellen und Hilfsmittel benutzt habe.

Heidelberg, den 20. September 2007

.....
Felix Frank